NACA

RESEARCH MEMORANDUM

INVESTIGATION AT TRANSONIC SPEEDS OF A

FORWARD-LOCATED UNDERSLUNG AIR INLET

ON A BODY OF REVOLUTION

By P. Kenneth Pierpont and John A. Braden

Langley Aeronautical Laboratory
Langley Field, Va.

NATIONAL ADVISORY COMMITTEE
FOR AERONAUTICS
WASHINGTON

January 29, 1953
Declassified November 8, 1957

NATIONAL ADVISORY COMMITTEE FOR AERONAUTICS

RESEARCH MEMORANDUM

INVESTIGATION AT TRANSONIC SPEEDS OF A

FORWARD-LOCATED UNDERSLUNG AIR INLET

ON A BODY OF REVOLUTION

By P. Kenneth Pierpont and John A. Braden

SUMMARY

An investigation was conducted in the Langley 8-foot transonic
tunnel to determine the flow phenomena, pressure recovery, and external
drag of a forward-located underslung air scoop mounted on a basic body
of revolution with fineness ratio 11, which when cut off to provide
an exit for the internal flow had a fineness ratio of 8. The forebody
was 4 diameters long and the minimum inlet area was 17.3 percent of the
frontal area. Both the basic body and the inlet body were tested through
a Mach number range from 0.6 to about 1.1 and an angle-of-attack range
from 0° to 10°. The inlet model was tested for mass-flow ratios from
about 0.2 to the maximum which would enter the inlet.

Results of the tests showed that the minimum external-drag coeffi-
cients occurred at maximum mass-flow ratios and were about equal to
those for the basic body for angles of attack to 10°. In the vicinity
of the maximum mass-flow ratio, the external-drag coefficients were
approximately the same as for an NACA 1-series nose inlet tested on a
similar afterbody. The external drag increased much more rapidly with
decreasing mass-flow ratio than for an open-nose inlet; the difference
in the effect of mass flow on external drag was explained by momentum
considerations. Total pressure recoveries exceeded 97 percent for all
Mach numbers and angles of attack for mass-flow ratios from 0.3 to
within 5 percent of the maximum and these recoveries exceeded those for
a comparable nose inlet at an angle of attack of 10°. Maximum test
mass-flow ratios were in good agreement with those calculated from one-
dimensional theory. Although pressure distributions indicated misaline-
ments of the inlet lip, no adverse effects on the external drag at high
mass-flow ratios are believed to have occurred.

INTRODUCTION

The instrumentation and armament requirements of military aircraft, fighter and interceptor types in particular, frequently require that engine air inlets be located on the sides of the fuselage. Engine-installation and internal-space-utilization specifications may lead to the use of either single or twin air scoops. No design selection data are available which are directly applicable to fuselage-side air inlets. One of the important variables, external lip shape, has been extensively investigated for axially symmetric air inlets and engine cowlings and the results reported in references 1 and 2 for low speeds and in references 3 and 4 for high speeds. Direct application of these data to the design of a scoop inlet, however, may not be satisfactory because of the lack of axial symmetry, the probable large differences in local angles of attack, and the interference effects at the lip-fuselage intersection. Results of such application were reported in reference 5 and compared with nose-inlet data of reference 1.

In order, therefore, to supply much-needed performance information concerning fuselage-side inlets in the high subsonic and transonic speed range, a test program was initiated in the Langley 8-foot transonic tunnel to study the effects on flow phenomena, pressure recovery, and drag of some of the more important geometric and aerodynamic variables. In order to ascertain the effects of inlet addition, a solid body was tested.

The inlet selected for this investigation consists of a forward-located single underslung scoop mounted 4.8 inches from the nose of the 8-inch-diameter body. The minimum inlet area was selected to be about 17 percent of the frontal area. This selection corresponds closely to the requirements for a turbojet-powered airplane designed for operation at an altitude of 35,000 feet, an inlet mass-flow ratio of about 0.8, and a Mach number of 0.95. For the details of this design, use was made of data believed applicable to the design of scoops contained in references such as 2 and 4.

Measurements were made on the basic body of the axial and normal forces together with pitching moments. Pressure distributions on the model and tunnel wall also were obtained. Measurements on the scoop body configuration included normal force, axial force, pitching moment, pressure recovery, mass flow, internal drag, and surface pressures on the several inlet components. Data were obtained for a Mach number range from 0.6 to 1.1 and at angles of attack from 0° to 10°.

SYMBOLS

C_{D_e} external-drag coefficient,

$$\left(\frac{G_a}{q_o F} + P_B \frac{B}{F} + C_{F_n} \right) \cos \alpha + \frac{G_n}{q_o F} \sin \alpha$$

C_{D_P} pressure-drag coefficient, $\displaystyle\int \frac{p - p_o}{q_o} d\left(\frac{r}{R}\right)^2$

C_{D_S} scoop incremental drag coefficient,

$$\left[\frac{p_p - p_o}{q_o} + 2c'\left(\frac{V_p}{V_o} - \frac{1}{\cos \alpha} \right) \right] \frac{A_p}{F} \cos \alpha$$

C_{F_n} internal-force coefficient, $\displaystyle\int c'_{F_n} d\frac{A_3}{F}$

C_L external lift coefficient,

$$\frac{G_n}{q_o F} \cos \alpha - \left(\frac{G_a}{q_o F} + P_B \frac{B}{F} + C_{F_n} \right) \sin \alpha$$

C_m external pitching-moment coefficient taken about maximum diameter station, $\displaystyle\frac{G_m}{q_o FD}$

c' point mass-flow coefficient, $\displaystyle\frac{\rho V}{\rho_o V_o}$

c'_{F_n} point internal-force coefficient,

$$2c'\left(\frac{V_3}{V_o} - 1 \right) + \frac{p_3 - p_o}{q_o}$$

A duct area

B   base area

D   maximum body diameter

F   fuselage maximum cross-sectional area

F_n internal force (positive when thrust, negative when drag), $m\left(V_3 - V_o\right) + \left(p_3 - p_o\right)A_3$

G_a, G_n, G_m strain-gage-measured axial force, normal force, and pitching moment

H   total pressure

$\bar{H}$ mass-flow-weighted average total pressure

h   inlet height

L   model length, taken without tail cone

M   Mach number

m   mass-flow rate, ρVA

m/m_o mass-flow ratio, $\dfrac{m}{\rho_o V_o A_1}$

p   static pressure

P   static-pressure coefficient, $\dfrac{p - p_o}{q_o}$

q   dynamic pressure, $\frac{1}{2}\rho V^2$

R   body maximum radius

r   radius

R_N Reynolds number

V   velocity

α angle of attack

γ ratio of specific heats, 1.4

θ meridian angle

ρ mass air density

Subscripts:

o   free stream

1   minimum area near inlet

2   diffuser measurement station

3   model exit

B   model base

l local

p   projection of area of inlet at leading edge

APPARATUS AND MODELS

Wind Tunnel and Model Support

The Langley 8-foot transonic tunnel, in which these tests were conducted, has a dodecagonal slotted test section and permits continuous testing up to a Mach number of about 1.1. Details of the test section are given in reference 6, and the aerodynamic properties of the air stream are reported in reference 7.

A sketch of the scoop model mounted in the tunnel is shown in figure 1 at 0° and 10° angle of attack and views of the basic body and the inlet models are shown mounted in the tunnel in figure 2.

General Arrangement

In order to facilitate the tests, two alternate afterbodies were used; hereinafter referred to as the "force" and "pressure" afterbodies. To insure that the force data would be free from mechanical interference, most of the pressure tubes required to obtain pressure distributions and duct performance were eliminated from the force afterbody. Figure 3(a) is a section view showing details of the solid nose mounted on the pressure afterbody, and figure 3(b) shows a cutaway sketch of the

scoop forebody mounted on the force afterbody. Figure 3(c) shows the details of the tail cone used on the force afterbody with the solid nose. The afterbodies were constructed principally of sheet aluminum, screw and rivet fastened; whereas the forebodies, figure 3(d), were constructed of multiple laminations of glass cloth bonded with phenolic-resin plastic.

Basic Body

The solid body shape selected, figure 3(a), had a forebody length of 4D and an afterbody length of 7D. From a point on the body 4 diameters behind the maximum, the body consisted of a straight cone to the point of body-sting intersection. Nondimensional coordinates for the general transonic fuselage reported in reference 8 were used to obtain the 8-inch-diameter basic body, coordinates for which are given in table I.

Scoop Model

The inlet model, shown in figures 2(b) and 3(b) had an underslung scoop, the leading edge of which was located 4.8 inches rearward of the nose of the forebody. In order to facilitate the installation of an inlet located so far forward, the body nose was raised 0.8 inch (see fig. 4(a)). Coordinates for the external body shape are given in table II.

The inlet area defined by the plane of the lip leading edge and the body was about $0.19F$, whereas the minimum area near the inlet was $0.173F$. Details of the inlet shape and lip section are given in figure 4(a). Downstream of the elliptical inner lip fairing, the duct area was held approximately constant for 2.8 inches (1.2h). The duct area then increased, as shown in figure 4(b), to 2.2 times the minimum at the inlet. Ducting in the afterbody was controlled largely by the instrumentation requirements together with provision for later tests of other scoop configurations which will utilize boundary-layer control (see fig. 3(b)).

During the initial test, the seams joining the lower lip section to the side sections of the inlet separated and resulted in the loss of the lower lip. After repair it was found that the lip drooped slightly, and is indicated by the dashed lines in figure 4(a). The maximum droop occurred at the vertical center line, was about 0.10 inch or equivalent to a change in lip angle of about 0.4°, and was thought to have had no significant effect on the results.

Instrumentation

Force measurements were obtained from a three-component (axial force, normal force, and pitching moment) calibrated strain-gage balance housed in the force afterbody shown in the cutaway sketch of figure 3(b). To insure measurement of all internal aerodynamic forces on the balance, the sting and balance were shielded by the fairing shown in the figure. An electrical fouling device was installed to detect fouling behind the strain-gage mounting.

Regulation of the internal mass rate of air flow was obtained by a remotely controlled throttle valve (see fig. 3), which consisted of eight radially located vanes which were rotated about their midchord in alternately opposite directions by a motor-actuated linkage. Measurement of the internal mass rate of air flow and internal drag was obtained with the aid of a cruciform exit rake of static- and total-pressure tubes shown in figures 3(b) and 5(a). Manual rotation of the rake on the sting permitted surveys of the jet flow. Rakes located in the ducting at the front of the pressure afterbody, station 32, enabled the determination of the internal total- and static-pressure recovery (see figs. 3(a) and 5(b)), and permitted a numerical check on the accuracy of the mass-flow measurements at the exit station. Rakes of total- and static-pressure tubes also were mounted in the diffuser of the force afterbody to assist in setting the mass-flow rate (see figs. 3(b) and 5(c)).

Measurements were made of the surface-static pressures on both models. On the solid nose, five radially located rows of orifices were installed (see table III). On the scoop forebody, measurements were made on the top, the ramp, the gutter, the outside of the lip, and the inside of the lip (see table IV). Pressures within the sting fairing were measured with the aid of a static-pressure tube located in the throttle motor well (see fig. 3(a)). Measurements of the tunnel-wall static pressures were obtained on a line 30° from the top center line (panel 11, ref. 7).

All pressure data were recorded photographically from multiple-tube manometers filled with tetrabromoethane. Force data were manually recorded from sensitive dial potentiometers and tunnel total temperatures were obtained from recording millivoltmeters. Flow visualization in the vicinity of the models was obtained in the form of schlieren photographs.

TESTS AND METHODS

Tests

For all the tests, the model nose was located approximately 37 inches downstream of the tunnel slot origin. Force and pressure data were

obtained for Mach numbers from about 0.6 to the maximum obtainable, about 1.1, and for angles of attack of 0° and about 4°, 7°, and 10°. For the solid model, data were obtained with and without the tail cone. For the inlet model, the mass-flow ratio was varied from about 0.2 (throttle closed) to the maximum which would pass through the inlet. The range of test Reynolds numbers is shown in figure 6.

Reduction of Data

Utilization of card punch-type computing machinery greatly facilitated the reduction of data to "point" values in the case of mass-flow and internal-force coefficients. The following two relations were used:

$$c' = \left[\frac{M_o}{\left(1 + \frac{\gamma-1}{2} M_o^2\right)^{1/2}}\right] \left[M\left(1 + \frac{\gamma-1}{2} M^2\right)^{1/2}\right] \times \left(\frac{1}{M_o^2} + \frac{\gamma}{2} \frac{p - p_o}{q_o}\right) \qquad (1)$$

$$c_{F_n}' = 2c'_3 \left\{\frac{\left[\dfrac{M_3}{\left(1 + \frac{\gamma-1}{2} M_3^2\right)^{1/2}}\right]}{\left[\dfrac{M_o}{\left(1 + \frac{\gamma-1}{2} M_o^2\right)^{1/2}}\right]} - 1\right\} + \frac{p_3 - p_o}{q_o} \qquad (2)$$

The Mach number functions in brackets were tabulated on a set of master cards as functions of p/H for use by the computers.

Mass-flow-weighted average total-pressure ratios were calculated numerically utilizing point values of c' from the relation:

$$\frac{\bar{H}_2}{H_o} = \frac{\sum\limits_1^n \frac{H_2}{H_o} c'_2 \Delta A_2}{\sum\limits_1^n c'_2 \Delta A_2} \qquad (3)$$

Mechanical and numerical integrations of this relation indicated maximum differences of ± 0.003. Comparisons of mass flow determined from measurements at the 32-inch station and the 64-inch station showed agreement

within ±0.01. The accuracy of the data is believed to be approximately as indicated:

p/H_O and H/H_O . . . . ±0.002

M_l . . . . ±0.006

M_O . . . . ±0.01

m/m_O . . . . ±0.01

$\alpha_{measured}$, deg . . . . ±0.1

Except for the wind-tunnel-wall effects, which will be discussed later, the force data are believed to lie within the following limits:

C_{D_e} . . . . ±0.01

C_L . . . . ±0.01

C_m . . . . ±0.02

Included in the estimated errors of mass-flow ratio and internal-force coefficient are those which resulted from leakage into the sting fairing and which were determined from static tests. The second-order effect resulting from use of C_{F_n} cos α as a drag force has been neglected.

Effects of sting interference are believed negligible.

RESULTS AND DISCUSSION

Presentation of the results of these tests has been divided into two principal parts: the first consists of consideration of the aerodynamic characteristics of the flow about the basic body and the second, of the aerodynamic characteristics of the external and internal flow about and within the inlet body.

It was reported in reference 9 that the drag of bodies of revolution as large as 8 inches diameter at an angle of attack of 0° in the Langley 8-foot transonic tunnel was not significantly affected by tunnel boundary interference for subsonic Mach numbers and probably not at $M_O \approx 1.10$, at which the reflection of the bow shock from the boundary occurred near the maximum body diameter. The effects of the tunnel walls on drag as well as lift and pitching moment for such a large model at angles of attack other than zero, however, were not determined. To study some of the effects of angle of attack on the results of the present tests, wall Mach numbers along an upper panel and model surface Mach numbers along the top row of orifices were plotted for the four test angles of attack, and comparisons of the wall distributions were made for the tunnel-empty

condition. At subsonic speeds, model-induced wall-measured disturbances for the solid model and the inlet model at intermediate and high mass-flow ratios were of similar magnitude to those reported in reference 9, and angle of attack did not cause appreciable changes. At supersonic speeds, shock reflections from the tunnel boundaries may have caused the drag to differ appreciably from that in free air and the reflection pattern became unsymmetrical at angles of attack other than zero. The bow-wave location and shape, figure 7, and the reflection patterns were essentially similar for the inlet body at the higher mass-flow ratios and the basic body, so that comparisons should afford a reasonably accurate indication of the drag increment. The accuracy of this drag increment should improve somewhat with increases in Mach number as the reflected shock moves back behind the maximum diameter.

The magnitudes of the effects of partly open tunnel boundaries on lift and pitching moment are not readily determined. It is obvious, however, that comparisons of data for the ducted model and solid model are valid for those cases wherein the flow fields a few diameters away are essentially identical.

Basic Body

Surface pressure distributions.- Pressure distributions along the top center line of the basic body $(\theta = 0^{\circ})$ are shown for 0° and 10° angle of attack in figure 8; also shown are distributions at $\alpha = 0^{\circ}$ for the basic body without tail cone. Irregularities in the distributions resulted primarily from constructional defects and are traceable through the Mach number range and for both angles of attack. A similar result was shown in reference 9 in which local surface irregularities were presented as supporting evidence. The general effect of increasing Mach number was to increase the percent of the total body load carried by the forebody, a result which applies for both angles of attack.

The general effect of increasing the angle of attack was to cause large decreases in the local pressures and corresponding changes in $\frac{dp}{dx}$ on the top of the forebody and small increases in the pressures over the top of the afterbody. Pressure recovery at $\alpha = 10^{\circ}$ over the afterbody was nearly as great as at $\alpha = 0^{\circ}$, and indicates that separation on the tail cone probably was not extensive. Although not presented, pressure distributions on the sides and bottom support this belief. Therefore, wall-reflected disturbances are believed to have affected only the pressure drag of the afterbody.

Drag.- External drag of the basic body configuration with and without tail cone consists of the base pressure force, corrected to free-stream static pressure, algebraically added to the measured drag; thus, external drag is the sum of the gage-pressure and viscous forces acting on the body surface to the point at which the body was cut off. External-drag coefficients together with the base-force coefficients

for the model with tail cone have been plotted as a function of stream Mach number for the four test angles of attack in figure 9; also in the figure are curves for angles of attack at 0° and 4° with the tail cone removed.

The variation of drag of the basic body with Mach number at 0° is essentially the same as that reported in reference 9. Fixing the transition 6.4 inches from the nose was shown by figure 13 of reference 9 (alternate model) to give no substantial drag increase; an indication that the flow was practically all turbulent anyway. Increasing the angle of attack to 4° did not result in any significant change in the external drag throughout the Mach number range (fig. 9(a)). For angles of attack of about 7° and 10°, substantial drag increases did occur at all Mach numbers; at $\alpha = 10.6^O$ and $M_O = 0.60$, the increase over the $\alpha = 0^O$ value amounted to about 0.05.

Removing the tail cone resulted in considerable increases in the measured balance force coefficient, figure 9(b). The differences in the measured force coefficients at the top of the figure are approximately the pressure drag of the tail cone shown in the middle plot. In the bottom plot of the figure, the external drag of the model without tail cone but corrected for the effect of tail-cone addition by algebraic addition of the pressure drag of the tail cone alone is compared with the basic body; the agreement is seen to be excellent.

Lift and pitching moment.- The variation of lift and pitching-moment coefficients as functions of stream Mach number is shown in figure 10. Portions of these data have been replotted in figure 11 on which have been included curves showing the variation with angle of attack of the lift and pitching-moment coefficients calculated according to the method of reference 10. The calculated normal-force-coefficient curve was assumed to be equal to the lift force for these low angles. The agreement between the test values and the calculated curve is considered good. Failure of the pitching moment to achieve anywhere near the theoretical value for $\alpha \approx 10^O$ probably resulted from boundary-layer separation of a different form than that assumed by the theory.

<div align="center">Underslung Scoop Model</div>

Flow into the inlet.- Study of the characteristics of the flow into the inlet was rendered possible by measurement of surface static pressures at the lateral plane of symmetry on the approach ramp and inner wall of diffuser (see figs. 12 to 15) and on the inside of the inlet lip (see fig. 16). Additional information was obtained of the flow field by means of the schlieren photographs, figure 7. The flow along the ramp into the inlet is characterized by three distinguishing features. These features are illustrated at $\alpha = 0^O$ in figure 12(a) as: (1) continuously accelerating flow into the duct, $\frac{m}{m_O} = 1.18$; (2) rapidly

accelerating flow on the fore section followed by a region of deceler-
ation near the inlet and which then reaccelerated as it approached the
minimum area $\frac{x}{L} \approx 0.12$, $\frac{m}{m_O} = 0.89$; and (3) rapid initial acceleration
followed by a general decelerating flow, $\frac{m}{m_O} = 0.24$.

Continuously accelerating flows occurred only at low stream Mach
numbers where the maximum mass rate of air flow into the inlet was con-
siderably greater than the flow in the stream per unit area $\left(\frac{m}{m_O} > 1.0\right)$,
$M_O = 0.60$ and 0.80. For these cases, the stagnation field of the
inlet lip moved well below and around the outside of the leading edge;
this decelerated field, therefore, did not importantly affect the flow
at the ramp surface. The lip in this case may be visualized as an air-
foil operating at a negative angle of attack. No difficulties may be
anticipated from the boundary layer, at least to the minimum area sta-
tion at the plane of symmetry. Downstream of the inlet within the duct,
the flow continued to accelerate to the effective minimum area $\left(\frac{x}{L} \approx 0.12\right)$
where sonic speeds were reached. Because of the ability in this model
to reduce the back pressure further, relatively large supersonic veloc-
ities resulted and were accompained by a system of strong shocks in the
diffuser. The existence of these shocks, of course, accounted for the
poor static pressure recovery for all chocked cases (see fig. 12).

Flows having two regions of acceleration occurred for intermediate
mass-flow ratios, $0.75 \leqq \frac{m}{m_O} \leqq 1.0$, at all stream Mach numbers and angles
of attack. Following an initial acceleration corresponding approximately
to that on the basic body, the flow decelerated from the ramp pressures
to meet the entrance conditions and the flow around the lip leading edge
shifted so that the stagnation point was inboard of the leading-edge
line; hence, the lip corresponded to an airfoil operating at positive
angles of attack. Small regions of boundary-layer separation may have
occurred near the corners where the lip and body intersect, because of
the strong adverse pressure gradient required to reach a stagnation con-
dition at the lip leading edge. Such regions of separated flow will
increase in importance as the mass-flow ratio is decreased. Separation
in the corners similar to that at low mass-flow rates, fluctuating flow,
or the rapid rate of change of static pressure with mass flow near
choking values could account for the pressure reversals shown in the
curves of the highest mass-flow ratios in figure 12, for example, see
$\frac{m}{m_O} = 0.99$ and 0.97, fig. 12(e)).

Flows having only one decelerating region were observed only at the
lower mass-flow ratios, $\frac{m}{m_O} < 0.75$, and at $\alpha = 0^O$ appear to have
resulted in boundary-layer separation at the ramp center line ahead of
the inlet station $\left(\frac{x}{L} = 0.075\right)$. Flow separation would be expected to
occur first from the upper wall of the diffuser well downstream of the

inlet, as was indicated in reference 11 for inlets with an appreciable boundary layer entering on one wall. A gradual loss of diffuser efficiency would therefore be expected at the lower mass-flow rates. The existence of such increased duct losses is indicated in figure 12(c) where the static pressure at the ramp center line just inside the inlet is seen to have decreased at $\frac{m}{m_0} \approx 0.23$, and then did not recover to as great a pressure ratio as at a much higher mass-flow rate; that is, $\frac{m}{m_0} = 0.54$.

Operation of the model at supersonic speeds merely resulted in the formation of a strong bow shock ahead of the model nose; and in no instance did the flow accelerate on the ramp ahead of the plane of the inlet to near sonic speeds. The effect of operation at the supersonic speeds of these tests then simply is equivalent to the inlet being placed in a subsonic stream corresponding approximately to the downstream Mach number of the bow shock with the total pressure loss equivalent to that across a normal shock. Movement and change of shape of this bow shock is shown in the schlieren photographs of figure 7(b). The bow wave ahead of the model nose at $M \approx 1.04$ is visible only at $\frac{m}{m_0} = 0.98$. The relatively wide band seen approaching the nose at this Mach number and which appears on the ramp at $M_0 \approx 1.09$, $\frac{m}{m_0} = 0.24$ is the bow wave striking the viewing windows.

Operation at positive angles of attack up to 10° is shown in figures 13, 14, and 15 to have resulted in a general increase in the pressure ratios on the ramp. Such an increase decreases the amount of deceleration at moderate mass-flow ratios required to meet the entrance conditions and increases the amount of acceleration near the inlet at high mass-flow ratios. As the angle of attack increased to 10°, separation of the boundary layer at the center line at low mass-flow rates, which occurred at $\alpha = 0^\circ$, seems to have disappeared because of the reduced maximum velocities and possibly because of cross flows which carried much of the boundary layer around the nose. The flow around the inside of the lip, figure 16, became supersonic for the highest test mass-flow ratio at $\alpha \approx 10^\circ$, even at the lowest Mach number of 0.6. It is not believed that extensive separation followed this supersonic bubble. Inner-lip studies to determine optimum shapes to reduce or eliminate such bubbles at high mass-flow rates are needed.

In general, improvements in the flow on the body ahead of the inlet are possible by reductions in the local curvature which would prevent the high local velocities ahead of the inlet shown at all moderate mass-flow rates and which, at the lower mass-flow rates, resulted in boundary-layer-separation losses at the plane of symmetry. Operation at the present low supersonic speeds caused no adverse flow conditions, and operation at positive angles of attack gave favorable flow changes. Operation at higher supersonic speeds, however, may cause serious adverse effects.

Maximum mass-flow rate.- Maximum obtainable mass-flow rates have been plotted as a function of stream Mach number in figure 17. It is seen that the flow rates closely approached the one-dimensional calculated values. Such a result is readily accounted for by the growth of the boundary layer along the approach ramp and inside the inlet to the entrance of the diffuser at about $\frac{x}{L} = 0.12$.

Flow around inlet.- Static pressure distributions at the center line of the outside lip are presented in figures 18 to 21 and along the line forming the intersection of the lip and the body surface in figures 22 to 25; this latter line is hereinafter referred to as the "gutter."

At an angle of attack of 0° and the maximum obtainable mass-flow rate, the static pressure near the leading edge along the center line decreased rapidly with stream Mach number and became supersonic between $M_O = 0.80$ and $M_O = 0.95$. At stream Mach numbers of 0.95 and greater, except possibly 1.09, this region of supersonic flow appears to terminate in a normal shock (see figs. 18(b) to 18(c)). At the lowest mass-flow rates and subsonic Mach numbers of 0.80 and 0.95 the region of supersonic flow also appears to terminate in a normal shock; however, for $M_O \geq 1.0$, a single normal shock does not seem possible from the pressure distributions.

Substantial decreases at maximum mass-flow ratios in local velocities over the surface occurred as the angle of attack was increased to 10° (compare figs. 18 to 21). At $\alpha = 0^{\circ}$, critical pressures were not reached for maximum mass-flow rates forward of $\frac{x}{L} \approx 0.12$ over the test range of Mach numbers; only gradual flow accelerations behind this point to the pressure required by the body are shown. No compression shocks near the inlet existed for these high mass-flow rates even for supersonic test Mach numbers. For the subsonic Mach numbers shown at $\alpha \approx 10^{\circ}$, a reduction in the mass-flow rate to as low as about 0.65 did not result in supersonic velocities on the lip outside. However, for $\alpha \approx 4^{\circ}$, $\frac{m}{m_O} = 0.60$ and at $M_O = 0.95$, a strong lambda shock is shown on the lip in figure 7(c). For $M_O = 1.00$, no compression can be seen in this figure for $\frac{m}{m_O} = 0.93$ but a small tail shows at $\frac{m}{m_O} = 0.61$. At $M_O = 1.04$, a normal shock from the lip is visible for the highest mass-flow rate but none is seen for $\frac{m}{m_O} = 0.76$ or 0.55. These photographs apparently substantiate the conclusion that at the supersonic test Mach numbers and the lowest mass-flow rates recompression seems to have occurred without a strong shock, but that at subsonic stream velocities and low mass-flow rates the supersonic region terminated in a normal shock.

Pressure distributions along the gutter are shown in figure 22 for $\alpha = 0^{\circ}$. The flow along the approach ramp controlled the pressures

forward of about $\frac{X}{L}$ = 0.06; behind this point the pressures on the lip leading edge for low and high mass-flow ratios controlled the ramp pressures. The compression shocks indicated at the center line on the outside of the lip at low mass-flow ratios for the subsonic flow cases appear from this figure to have extended around the entire lip periphery. At the highest angle of attack, it is seen that substantial reductions in local Mach numbers at high mass-flow rates did not occur behind the lip leading edge $\left(\text{that is, } \frac{X}{L} \approx 0.10\right)$; a result opposite to that found for the lip center line. In fact, comparison of figure 22 with figure 25 shows that an increase in the maximum local Mach number has occurred at the high mass-flow ratios. This increase was caused by an increase in the angle of attack of the end sections and the unfavorable effects of the lip-fuselage junction.

The conclusion from these data is that the lip was not well-alined with the flow field of the body by perhaps 10°. One way to design the scoop lip would be to calculate the streamline pattern of the body and to aline the lip with this flow. At the end sections allowance should be made for the adverse angle-of-attack and fuselage-juncture effects.

Flow on top of body.- Pressures along the top of the model at the plane of symmetry for the maximum mass rate of air flow are shown for the four test angles of attack in figure 26. A more rapid flow acceleration occurred on the forward portions than on the basic body (compare with fig. 8) and was followed by a small compression. This compression occurs in the region of reduced body curvature brought about by applying the basic body ordinates to the S-curved center line employed to raise the nose 0.8 inch (see fig. 4). Critical pressures were reached for about the same stream Mach number and changes with angle of attack were similar in magnitude to the basic body. Comparison of the flow over the afterbody for either high or low mass-flow ratios, figure 26(a), with that for the basic body without tail cone, figure 8(c), shows that most of the effect of internal flow is felt only on the rear 10 percent of the body length. A similar result was shown in reference 12. In general the effect of the internal flow was to raise the pressures on the afterbody and thereby reduce the external drag.

Pressure recovery.- The variation of mass-flow-weighted total-pressure ratio at the end of the 2.2/1 area-ratio diffuser, as a function of mass-flow ratio at an angle of attack of 0°, is presented in figure 27. The maximum recovery is indicated to be greater than 99 percent for all Mach numbers and occurs near $\frac{m}{m_o}$ = 0.55. As the mass-flow rate was decreased, the recovery remained above 98 percent down to $\frac{m}{m_o}$ = 0.30 for all test Mach numbers. At the high mass-flow rates, to within about 5 percent of the maximum obtainable flow rate, the total pressure decreased slowly but remained above $0.97H_o$. This gradual decrease is

simply the usual frictional losses and can be adequately predicted by methods such as those of reference 13.

Angle-of-attack performance is shown in figure 28 where the pressure recovery is plotted against mass-flow ratio for four angles of attack and is shown for six representative stream Mach numbers. The total-pressure-ratio behavior above $\frac{m}{m_0} \approx 0.5$ was unaffected by angle of attack for all Mach numbers. Below this value, the recovery increases slightly with angle of attack until, at 10^0, the curve is flat from the minimum flow rate upwards. The flatness of this curve for $\alpha \approx 10^0$ is similar to that for an open nose inlet at 0^0; whereas, the slight decrease at low angles is associated with the boundary-layer separation on the ramp previously discussed. The abrupt decrease in recovery for all angles of attack near the maximum flow rate is generally characteristic of stagnation types of inlet without internal separation ahead of the minimum area.

The rate of static-pressure change with mass-flow ratio is shown in figure 29 for $\alpha = 0^0$ and in figure 30 for the four angles of attack. The relative performance of the diffuser, as it is affected by angle of attack, is shown in figure 31 in which the diffuser loss $\Delta H/q_1$ has been plotted as a function of mass-flow ratio. The curves show that there could not have been any appreciable separation within the diffuser above $\frac{m}{m_0} = 0.55$ at either angle of attack and that below this value separation which occurred at $\alpha = 0^0$ was appreciably reduced when the angle was increased to 10^0.

Internal performance also is indicated by the mass-flow and impact-pressure ratio contours at the diffuser measurement station shown in figures 32 and 33. For the lowest mass-flow rate the small differences in the total- and static-pressure tube readings precluded construction of accurate mass-flow contours; however, the contours of impact-pressure ratio shown give an adequate picture of the flow. At the intermediate and high mass-flow rates shown, impact pressure as well as the mass flow is greater in the two lower passages, which was expected because of the internal-duct design. In general, no important regions of flow distortion are shown.

Drag.- The definition of external drag for the inlet body is analogous to that for the solid body; it consists of all pressure and viscous forces on the external body surface and the entering stream-tube surface except those which are common to both surfaces. The breakdown of drag into internal and external forces has been discussed in references 14 and 15. The concept of scoop incremental drag was introduced in reference 16, wherein it was shown that algebraic subtraction of the scoop incremental drag from the external drag yields the sum of all pressure and viscous forces on all body surfaces including those washed by the entering flow.

The variation of external-drag coefficient as a function of mass-flow ratio is shown in figure 34; base- and internal-force coefficients are presented in figures 35 and 36, respectively. For $\alpha = 0^{\circ}$ the flagged symbols indicate reproducibility of the data. Comparison of figure 34 with figure 9 shows that the minimum drag for $\alpha = 0^{\circ}$, which occurred at the maximum flow rate, was approximately the same as that for the basic body for all test Mach numbers. It is therefore concluded that the lip misalinement indicated in a previous section has not adversely affected the external drag at high mass-flow ratios.

The external-drag-coefficient increase associated with mass-flow decrease has been plotted in figure 37 and compared with scoop incremental drag coefficient calculated from one-dimensional considerations using the inlet area defined by the stagnation line at the leading edge. The difference between the two curves when decreased by the pressure drag of the washed surface represents approximately the suction force developed on the inlet lip and is at least conservative. The rest of the calculated incremental-drag coefficient represents a measure of the inability, in a real fluid, of the scoop lip to realize the low static pressures required, of the change in pressure drag caused by the jet exit, and the changes in viscous drag on the entire body.

Isolation of the effects of the flow into the inlet on the external-drag coefficients obtained in most model investigations are subject to two sources of difficulty: first, the model exit area is much too large to represent a practical airplane installation and, second, the after-body surface pressures change as a result of cutting off the basic body and passing air through it. To give an indication of the magnitude of these effects, afterbody pressure-drag coefficients have been plotted in figure 38 for $\alpha = 0^{\circ}$ through the Mach number range for the basic body, basic body without tail cone, inlet body at low mass-flow rate, and inlet body at high mass-flow rate. The curves at supersonic Mach numbers are shown dashed because of the unknown effects of the wall-reflected disturbances in this range. The drag increase which results from removing the tail cone (compare with fig. 9(b)) is nearly that of the pressure drag of the tail cone alone; passing air through the model resulted in only small decreases in the pressure drag. Larger inlets and correspondingly greater mass flows or smaller exits for the same mass flows would probably give rise to larger changes in the afterbody pressure drags than observed in the present tests; therefore, dependence of the external pressure drag on the afterbody shape cannot be neglected.

Less extensive data were obtained at angles of attack, figure 34. Because of the failure of the base pressure tube at an angle of attack of approximately 7° and 10°, the corrections for $\alpha = 0^{\circ}$ were applied, figure 35. No serious error should result since the base pressure would be expected to be essentially independent of angle of attack. The trend is the same as was noted for $\alpha = 0^{\circ}$ and again the general conclusion

is reached that the minimum external drag is about equal to that for the basic body.

Lift and pitching moment.- Subject to the wind-tunnel wall effects, certain trends may be established concerning lift and pitching moments of the scoop model. External lift and external pitching moment include all effects of pressure and viscous forces on the external body surface and the entering stream tube surface, except those which are common to both surfaces. Lift and pitching-moment contributions which result from induction of air into a fuselage operating in a subsonic and low supersonic air stream cannot readily be separated in a manner similar to the drag forces; that is, those acting on the entering stream tube and those acting on the body surface.

External lift coefficient has been plotted as a function of mass flow in figure 39. From a comparison of the lift on the scoop model with that measured on the basic body, figure 9(a), at corresponding angles of attack and Mach numbers, it appears that the lift coefficient of the ducted body decreases to about the value for that of the basic body at zero mass flow. Furthermore, the slope of the lift curve increases with angle of attack.

Variation of external pitching moment for the underslung scoop is shown in figure 40 as a function of mass-flow ratio. Relatively large changes in mass-flow rate are shown to have resulted in only slight changes in pitching-moment coefficient, a result which is considered somewhat surprising in view of the variation of lift and drag with mass-flow ratio. In addition the changes in the loading brought about by changes in angle of attack have resulted in relatively unimportant changes in pitching moment if compared with the pitching moment of the basic body.

Comparison of performance of scoop model with nose inlet.- For the comparison of the over-all performance of several inlet configurations, both the external-drag and internal-pressure recovery must be considered. Comparison of the external-drag coefficients at a high mass-flow ratio $\left(\frac{m}{m_0} \approx 0.8\right)$, the change in external-drag coefficient with mass-flow ratio, and the pressure recovery of the scoop-type fuselage inlet of the present investigation with that for an NACA 1-40-200 and an NACA 1-40-400 nose inlet tested in the Langley 8-foot transonic tunnel on a similar afterbody, reference 15, are shown in figures 41, 42(a), and 43, respectively. Both of these nose inlets have approximately the same inlet area as the scoop model. Included in figure 42 are additional drag increment data for an NACA 1-50-200 (ref. 15) and an NACA 1-80-100 nose inlet with central body (from unpublished data taken in Langley 8-foot transonic tunnel).

The external drag of the scoop configuration, figure 41, is markedly lower than for the NACA 1-40-400 nose inlet at all subsonic Mach numbers.

Lack of data at the lowest Mach number for the 1-40-200 inlet prevents adequate comparison; however, if the curve trend is similar to the other nose inlet shown, no further drag reduction would be expected and the scoop and the NACA 1-40-200 inlet may be said to have about the same subcritical drag. The supercritical drag rise of the NACA 1-40-200 inlet occurs at a lower Mach number than the underslung scoop, and at a much more rapid rate than the NACA 1-40-400 inlet. At the highest test Mach number the external drag of the scoop inlet and the NACA 1-40-400 nose inlet are about the same. These results indicate that up to $M_O = 1.1$ the scoop inlet was at least as good dragwise at high mass-flow ratios as the NACA 1-series nose inlets of comparable inlet area.

A comparison of the external-drag increments, which result from operation at mass-flow ratios less than the maximum, is shown in figure 42(a) for four inlet configurations. The minimum area of the underslung scoop and the NACA 1-40-400 nose inlet are approximately the same, whereas that for the NACA 1-80-100 with an 0.47D elliptical central body lies between that for the NACA 1-40-400 and the NACA 1-50-200 open-nose inlets. It is shown that the external-drag-coefficient increment for both the nose inlets varies approximately linearly throughout the mass-flow range and amounted to only 0.02 at $\frac{m}{m_O} = 0.4$ and $M_O \approx 1.1$. However, for both the underslung scoop and the nose inlet with central body, important drag-coefficient increments in excess of that for the two open-nose inlets are indicated to have occurred (that is, $C_{D_e} - C_{D_{e_{min}}} \approx 0.06$; $\frac{m}{m_O} = 0.4$; $M_O \approx 1.1$).

The principal causes for the failure of the scoop-type inlet to achieve as small external-drag-coefficient increments at reduced mass-flow ratios as the open-nose inlet can be found by consideration of the momentum theorem. A three-dimensional control surface is selected which consists of the boundaries A, C, and E in figure 42(b). It may then be shown that the force obtained by integration of the pressures along the stream tube must, in an inviscid fluid, be equal and opposite in sign to the sum of the pressure forces on the lip and body.

A second control surface is selected which consists of the boundaries A, B, F, and G in figure 42(b). The change in total momentum of the entering flow from the free stream to the face of the inlet will be the same for any two inlets which have the same inlet area and which operate at the same mass-flow ratio. The difference between the force on the stream tube surface, and hence the body suction force, of a scoop inlet and a nose inlet is consequently equal to the force on the surface ahead of the scoop inlet which is washed by the entering flow. Since the washed surface does not constitute a closed body, a drag force must be experienced by this surface, even in an inviscid fluid; hence, the the body suction force for a scoop inlet would be required to exceed that for the comparable open-nose inlet. An exception for which the body

suction force required equals that for the nose inlet is that in which the scoop is located on a semi-infinite surface, or for the practical case in which the scoop is located far back on a nonexpanding body.

Most of the body suction force would be expected to be carried by the inlet lip itself; therefore, if the inlet-lip profiles are identical, lower local static pressures are required for the scoop than for the open-nose inlet. Furthermore, for the assumed lip contours, the projected frontal area of the lip for the scoop inlet is usually much less than for the open-nose inlet; hence, the local static pressures must be further decreased on the scoop. These lower required static pressures result immediately in much more severe viscous effects on the outside of the scoop than for the open-nose inlet. It would be expected, therefore, that the external drag for the scoop inlet will be greater than for the open-nose inlet. Furthermore, because the washed area for the open-nose inlet with central body is constant for all mass-flow ratios, the external drag for this configuration may be expected to be greater than for the scoop inlet. The experimental results shown in figure 42(a) are in agreement with the qualitative results obtained from the momentum theorem.

The internal total pressure recovery after diffusion at $\alpha = 0^O$ and for $\frac{m}{m_O} > 0.6$ is practically the same for all the inlets shown in figure 43. The loss in recovery felt by the nose inlets for $\alpha = 10^O$ resulted from extensive flow separation on the lower portion of the duct which is presumed to have occurred at the lip fairing. No significant amount of separation occurred in the scoop inlet. These data, together with the external-drag data, show that the performance of the underslung scoop was as good as for the open-nose inlet at medium and high mass-flow ratios at zero angle of attack.

CONCLUDING REMARKS

Results of an investigation at Mach numbers from about 0.6 to 1.1 in the Langley 8-foot transonic tunnel of a basic body and a forward-located underslung scoop model having an inlet area of 17.3 percent of the body frontal area indicate the following:

1. At an angle of attack of zero and a mass-flow ratio of 0.8, the external-drag coefficients and pressure recoveries of the underslung scoop were approximately equal to those for an NACA nose inlet of similar size. Total pressure recovery at an angle of attack of 10° was higher for the scoop model than for the nose inlet.

2. The external drag increased much more rapidly with decreasing mass-flow ratio than for an open-nose inlet; the difference in the effect of mass flow on external drag was explained by momentum considerations.

3. External-drag coefficients for the highest mass-flow rates were approximately equal to those for the basic body for angles of attack up to 10°. Misalinement of the inlet lip, indicated by pressure distributions, did not adversely affect the external drag at high mass-flow ratios.

4. Maximum test mass-flow ratios were in good agreement with those calculated for one-dimensional flow.

5. From mass-flow ratios ranging from about 0.3 to within 5 percent of the maximum, total pressure ratios at the end of a 2.2/1 area-ratio diffuser in excess of 97 percent were realized; operation at angles of attack resulted in no measurable changes at high mass-flow ratios but a slight increase at the lowest mass-flow rates.

6. Operation at positive angles of attack resulted in flow improvements on both the ramp and lower outside lip. At low mass-flow rates, separation of the boundary layer ahead of the inlet, which occurred for an angle of attack of 0°, was eliminated at an angle of attack of 10°. At high mass-flow rates, sonic velocities were not reached ahead of the inlet for any test Mach number at an angle of attack of 10°.

Langley Aeronautical Laboratory,
        National Advisory Committee for Aeronautics,
                Langley Field, Va.

REFERENCES

1. Baals, Donald D , Smith, Norman F., and Wright, John B.: The Development and Application of High-Critical-Speed Nose Inlets. NACA Rep. 920, 1948. (Supersedes NACA ACR L5F30a.)

2. Nichols, Mark R., and Keith, Arvid L., Jr.: Investigation of a Systematic Group of NACA 1-Series Cowlings With and Without Spinners. NACA Rep. 950, 1949. (Supersedes NACA RM L8A15.)

3. Pendley, Robert E., and Smith, Norman F.: An Investigation of the Characteristics of Three NACA 1-Series Nose Inlets at Subcritical and Supercritical Mach Numbers. NACA RM L8L06, 1949.

4. Pendley, Robert E., Robinson, Harold L., and Williams, Claude V.: An Investigation of Three Transonic Fuselage Air Inlets at Mach Numbers From 0.4 to 0.94 and at a Mach Number of 1.19. NACA RM L50H24, 1950.

5. Smith, Norman F., and Baals, Donald D.: Wind-Tunnel Investigation of a High-Critical-Speed Fuselage Scoop Including the Effects of Boundary Layer. NACA ACR L5B01a, 1945.

6. Wright, Ray H., and Ritchie, Virgil S.: Characteristics of a Transonic Test Section With Various Slot Shapes in the Langley 8-Foot High-Speed Tunnel. NACA RM L51H10, 1951.

7. Ritchie, Virgil S., and Pearson, Albin O.: Calibration of the Slotted Test Section of the Langley 8-Foot Transonic Tunnel and Preliminary Experimental Investigation of Boundary-Reflected Disturbances. NACA RM L51K14, 1952.

8. Thompson, Jim Rogers: Measurements of the Drag and Pressure Distribution on a Body of Revolution Throughout Transition From Subsonic to Supersonic Speeds. NACA RM L9J27, 1950.

9. Pendley, Robert E., and Bryan, Carroll R.: An Investigation of Some Factors Affecting the Drag of Relatively Large Nonlifting Bodies of Revolution in a Slotted Transonic Wind Tunnel. NACA RM L52H22, 1952.

10. Allen, Julian H.: Estimation of the Forces and Moments Acting on Inclined Bodies of Revolution of High Fineness Ratio. NACA RM A9I26, 1949.

11. Nichols, Mark R., and Pierpont, P. Kenneth: Preliminary Investigation of a Submerged Air Scoop Utilizing Boundary-Layer Suction to Obtain Increased Pressure Recovery. NACA RM L50A13, 1950.

12. Becker, John V.: Wind-Tunnel Investigation of Air Inlet and Outlet Openings on a Streamline Body. NACA Rep. 1038, 1951. (Supersedes NACA ACR, Nov. 1940.)

13. Beeton, A. B. P.: Curves for the Theoretical Skin Friction Loss in Air Intake Ducts. TN No. Aero 2035, British R.A.E., Feb. 1950.

14. Wyatt, De Marquis D.: Aerodynamic Forces Associated With Inlets of Turbojet Installations. Aero. Eng. Rev., vol. 10, no. 10, Oct. 1951, pp. 20-23, 31.

15. Pendley, Robert E., Milillo, Joseph R., and Fleming, Frank F.: An Investigation of Three NACA 1-Series Nose Inlets at Subsonic and Transonic Speeds. NACA RM L52J23, 1952.

16. Klein, Harold: The Calculation of the Scoop Drag for a General Configuration in a Supersonic Stream. Rep. No. SM-13744, Douglas Aircraft Co., Inc., Apr. 12, 1950.

TABLE I

DESIGN AND MEASURED FUSELAGE COORDINATES FOR 8-INCH-DIAMETER BASIC BODY

Design Coordinates		Measured Coordinates			
x, in.	r, in.	x, in.	r, in.	x, in.	r, in.
0	0	0.011	0	28.003	3.971
.320	0.222	0.999	.484	28.999	3.987
.480	.286	2.000	.819	29.996	3.996
.800	.411	2.997	1.097	30.751	3.996
1.600	.693	4.022	1.360	33.250	4.001
3.200	1.157	4.991	1.598	34.754	3.996
4.800	1.549	5.998	1.822	36.256	3.987
6.400	1.892	6.994	2.022	38.014	3.963
9.600	2.489	7.998	2.210	39.762	3.939
12.800	2.966	8.995	2.388	41.143	3.910
16.000	3.326	9.994	2.553	44.623	3.825
19.200	3.519	10.995	2.709	46.252	3.784
22.400	3.776	11.990	2.853	48.137	3.713
25.600	3.901	12.998	2.987	50.012	3.639
28.800	3.978	14.001	3.109	52.021	3.558
32.000	4.000	14.987	3.219	53.998	3.449
37.600	3.965	15.991	3.320	55.896	3.320
43.200	3.863	16.997	3.418	57.770	3.185
48.800	3.688	17.999	3.498	60.014	3.004
54.400	3.419	18.999	3.576	63.521	2.654
60.600	3.003	19.998	3.642	64.468	2.548
64.000	2.600	21.000	3.699	66.464	2.342
74.600	1.515	22.000	3.750	68.459	2.139
		23.000	3.796	70.463	1.932
		25.000	3.874	72.470	1.726
		25.995	3.913	73.819	1.587
		26.997	3.944	74.575	1.515

Note.- From 64.000 in. to 74.600 in., Conical Tail Fairing

NACA

TABLE II.- UNDERSLUNG SCOOP FOREBODY DESIGN COORDINATES

x, in.	$y_{C_L}^*$, in.	x, in.	r_t^*, in.	b, in.	r_b^*, in.
0	0.800	0	0	0	
.800	.799	0.120	0.134	0.134	
1.600	.796	.320	.222	.222	
3.200	.784	.480	.286	.286	
4.000	.775	.800	.411	.411	
4.800	.764	1.600	.693	.693	
6.000	.744	3.200	1.157	1.157	
8.000	.700	3.500	1.236	1.236	
10.000	.644	3.730	1.295	1.295	
12.000	.575	4.000	1.360	1.354	
14.000	.494	4.300	1.432	1.393	
16.000	.400	4.600	1.503	1.412	
18.000	.306	4.800	1.549	1.414	3.000
20.000	.225	4.852	1.559		3.066
22.000	.156	4.934	1.578		3.104
24.000	.099	5.068	1.609		3.147
26.000	.055	5.300	1.661		3.206
28.000	.016	5.739	1.755		3.295
30.000	0	6.000	1.810		3.339
32.000	0	6.142	1.840		3.361
		6.813	1.978		3.453
		2.500	2.108		3.528
		8.000	2.201		3.578
		10.000	2.555		3.736
		12.000	2.858		3.853
		14.000	3.112		3.934
		16.000	3.326		3.982
		18.000	3.502		3.999
		20.000	3.643		4.000
		22.000	3.756		4.000
		24.000	3.841		4.000
		26.000	3.915		4.000
		28.000	3.971		4.000
		30.000	4.000		4.000
		32.000	4.000		4.000

*See figure 4a.

TABLE III

MEASURED LOCATIONS OF SURFACE ORIFICES ON BASIC MODEL

x, in.					
$\theta = 0^\circ$	$\theta = 0^\circ$ cont'd.	$\theta = 45^\circ$	$\theta = 90^\circ$	$\theta = 135^\circ$	$\theta = 180^\circ$
0.01	27.00	1.98	1.99	1.99	2.00
1.00	28.00	4.00	3.98	3.94	4.00
2.00	29.00	5.99	5.98	6.00	5.99
3.00	30.00	7.99	7.99	8.00	8.00
4.02	30.75	10.00	9.99	9.99	10.00
4.99	33.25	11.99	11.99	11.99	11.99
6.00	34.75	13.99	13.99	14.00	14.00
6.99	36.26	16.00	15.99	15.99	16.00
8.00	38.01	18.00	17.99	17.99	18.00
9.00	39.76	20.00	20.00	19.99	19.99
9.99	41.14	22.00	22.00	21.99	21.99
11.00	44.62	24.00	24.00	23.99	24.00
11.99	46.25	25.99	25.99	25.99	25.99
13.00	48.14	28.00	28.00	27.99	27.99
14.00	50.01	30.00	30.00	29.99	29.99
14.99	52.02		33.25		33.25
15.99	54.00		36.27		36.28
17.00	55.90		39.76		39.77
18.00	57.77		44.62		44.62
19.00	60.01		48.14		48.14
20.00	63.52		52.00		52.02
21.00	64.47		55.90		55.89
22.00	66.46		60.02		60.03
23.00	68.46		63.51		63.52
24.00	70.46		64.48		
25.00	72.47		68.47		
26.00	73.82		72.46		
			73.81		

NACA

TABLE IV

MEASURED LOCATIONS OF SURFACE ORIFICES ON SCOOP FOREBODY

x, in.				
Top	Ramp	Gutter	Lip, inside	Lip, outside
0	1.00	2.01	5.04	4.80
3.99	1.49	3.00	5.28	5.04
8.00	2.00	3.99	5.52	5.28
11.99	2.51	4.80	5.76	5.52
16.01	3.01	5.99	6.23	5.76
20.00	3.49	8.00		6.23
23.99	4.00	10.01		6.71
28.00	4.81	12.01		7.67
30.50	5.50	14.01		9.58
	5.99	16.00		11.49
	7.01	19.99		13.50
	8.00	23.99		14.00
	10.00			15.99
	12.00			18.01
				20.00 *
				22.01
				24.01
				26.01
				28.01
				30.00

*End of NACA 1-series cowl ordinates

NACA
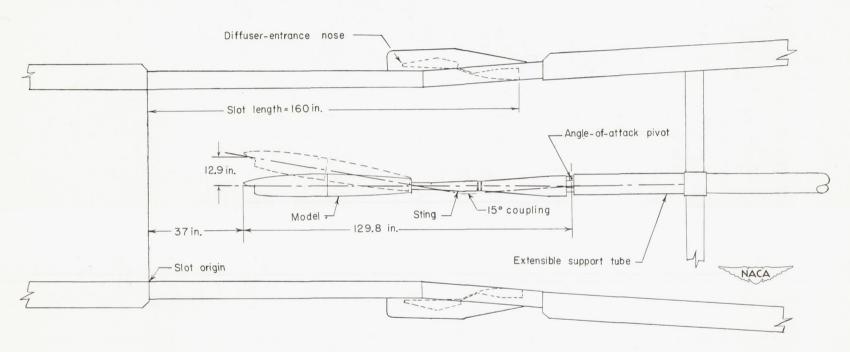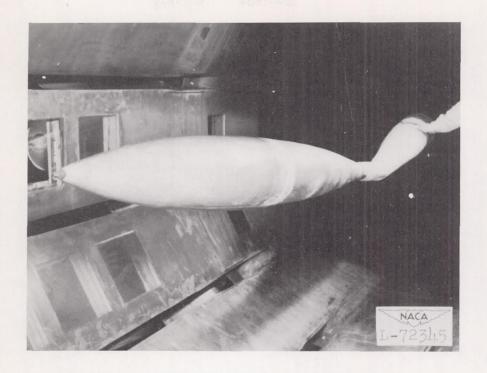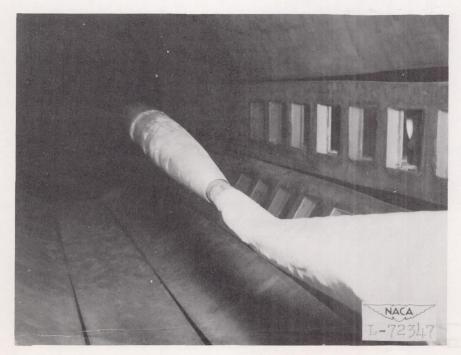
Figure 1.- General arrangement of inlet model mounted in the Langley
8-foot transonic tunnel.
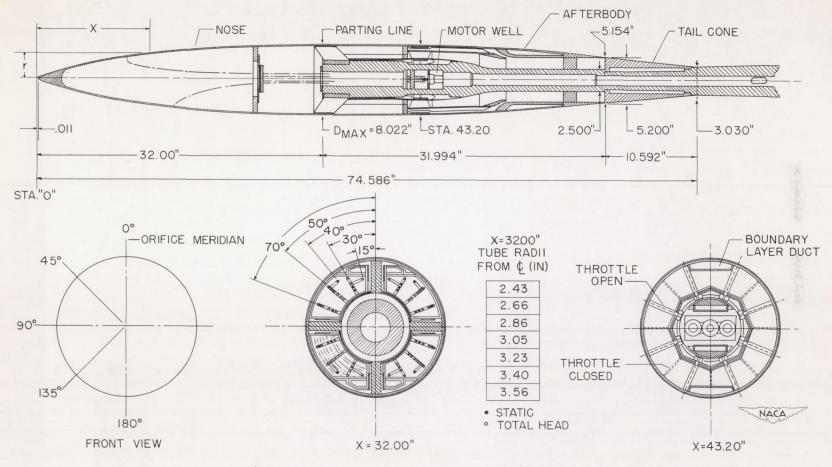
(a) Solid nose on force afterbody.

Figure 2.- Basic body and inlet model mounted in tunnel.
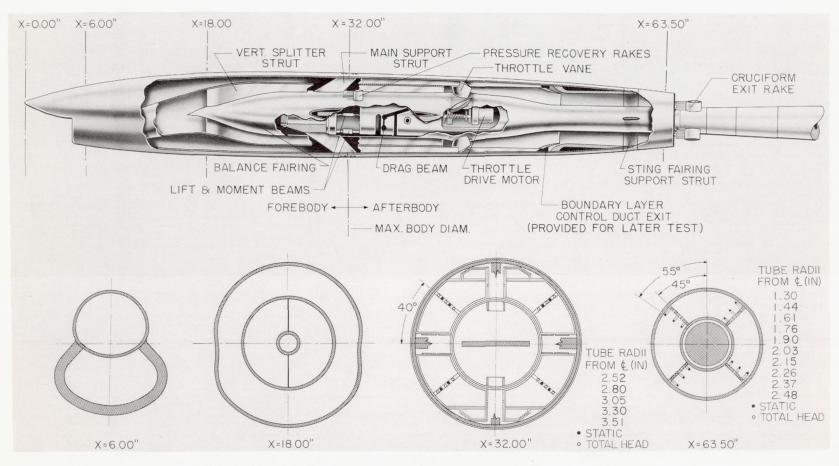
(b) Underslung scoop on pressure afterbody.

Figure 2.- Concluded.

FRONT VIEW

X = 32.00"

X=43.20"

X=32.00" TUBE RADII FROM ₵ (IN)		
2.43		
2.66		
2.86		
3.05		
3.23		
3.40		
3.56		

• STATIC
○ TOTAL HEAD

(a) Solid nose on the pressure afterbody.
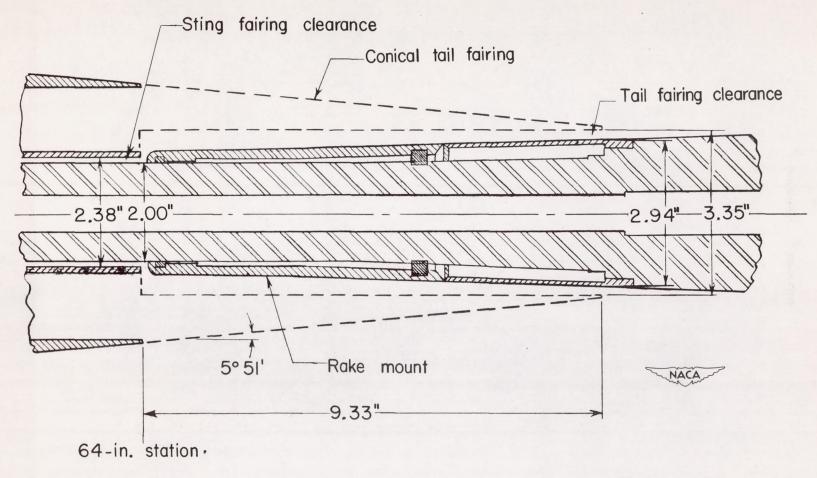
Figure 3.- Forebodies and afterbodies used in the investigation.
(All dimensions in inches.)

X=0.00" X=6.00" X=18.00 X=32.00" X=63.50"

VERT. SPLITTER STRUT MAIN SUPPORT STRUT PRESSURE RECOVERY RAKES

THROTTLE VANE

CRUCIFORM EXIT RAKE

BALANCE FAIRING DRAG BEAM THROTTLE DRIVE MOTOR STING FAIRING SUPPORT STRUT

LIFT & MOMENT BEAMS

FOREBODY AFTERBODY

MAX. BODY DIAM.

BOUNDARY LAYER CONTROL DUCT EXIT (PROVIDED FOR LATER TEST)

X=6.00" X=18.00" X=32.00" X=63.50"

40°

TUBE RADII FROM ₵ (IN)
2.52
2.80
3.05
3.30
3.51
• STATIC
○ TOTAL HEAD

55°
45°

TUBE RADII FROM ₵(IN)
1.30
1.44
1.61
1.76
1.90
2.03
2.15
2.26
2.37
2.48
• STATIC
○ TOTAL HEAD

(b) Underslung scoop on the force afterbody.

Figure 3.- Continued.

NACA

L-77033

Sting fairing clearance

Conical tail fairing

Tail fairing clearance

2.38" 2.00"

2.94" 3.35"

5° 51'

Rake mount

9.33"

64-in. station
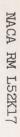
(c) Force-model tail fairing.
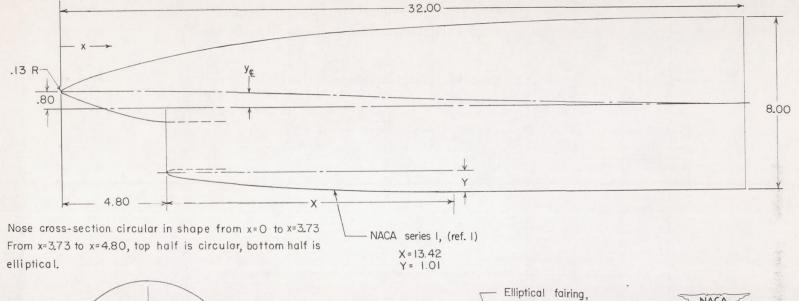
Figure 3.- Continued.
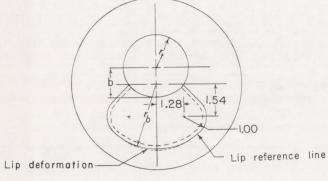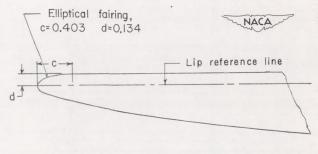
(d) Photograph of solid nose and underslung scoop.

Figure 3.- Concluded.

Nose cross-section circular in shape from x=0 to x=3.73
From x=3.73 to x=4.80, top half is circular, bottom half is
elliptical.

NACA series I, (ref. I)

X = 13.42
Y = 1.01

Elliptical fairing,
c=0.403 d=0.134

Lip reference line

Lip deformation

Lip reference line
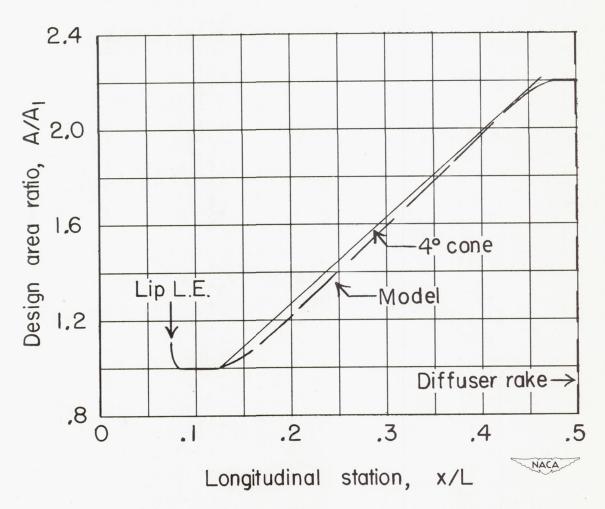
Inlet dimensions
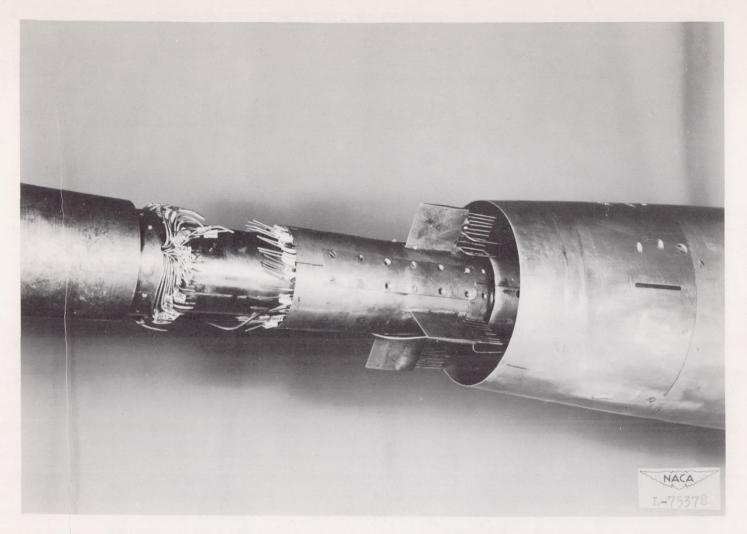
(a) Inlet and lip dimensions.   (All dimensions in inches.)

Figure 4.- Details of underslung scoop.

(b) Variation of internal ducting area in scoop forebody.
A_1 = 8.70 square inches.

Figure 4.- Concluded.
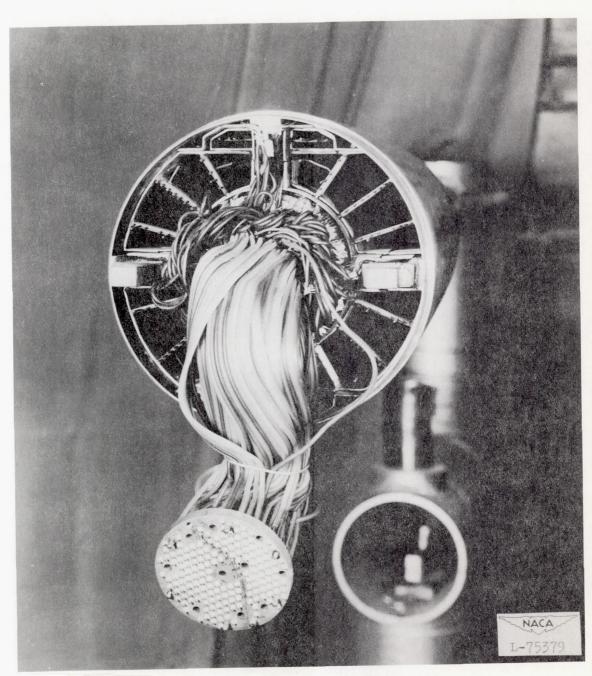
(a) Exit rakes on force afterbody.

Figure 5.- Flow measurement rakes.
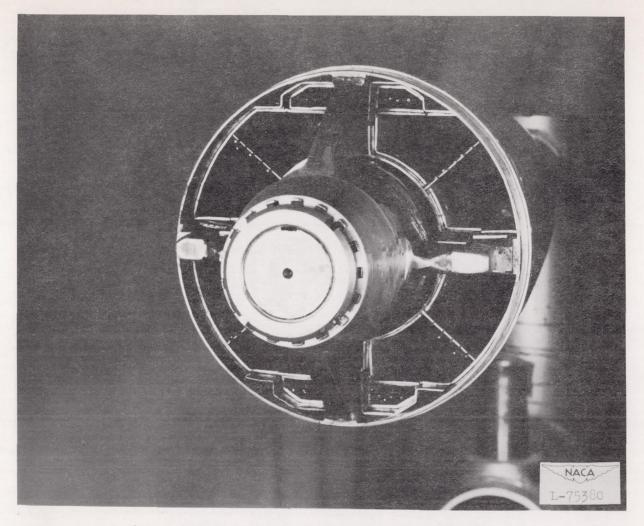
(b) Pressure-recovery rakes on pressure afterbody.

Figure 5.- Continued.

(c) Pressure-recovery rakes on force afterbody.

Figure 5.- Concluded.
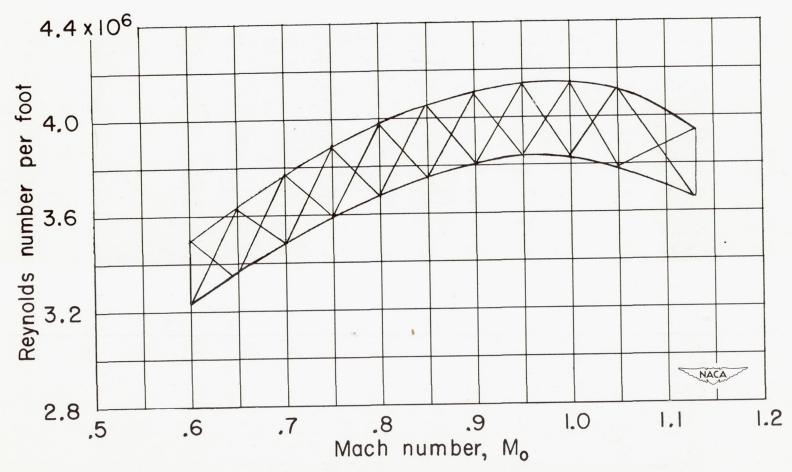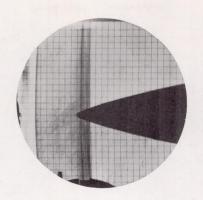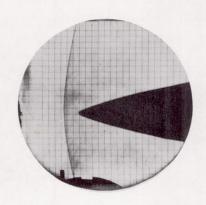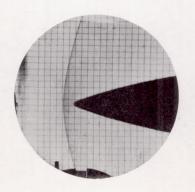
Figure 6.- Reynolds number variation per foot lineal dimension in the
Langley 8-foot transonic tunnel.

$M_0 = 1.05$

$M_0 = 1.07$
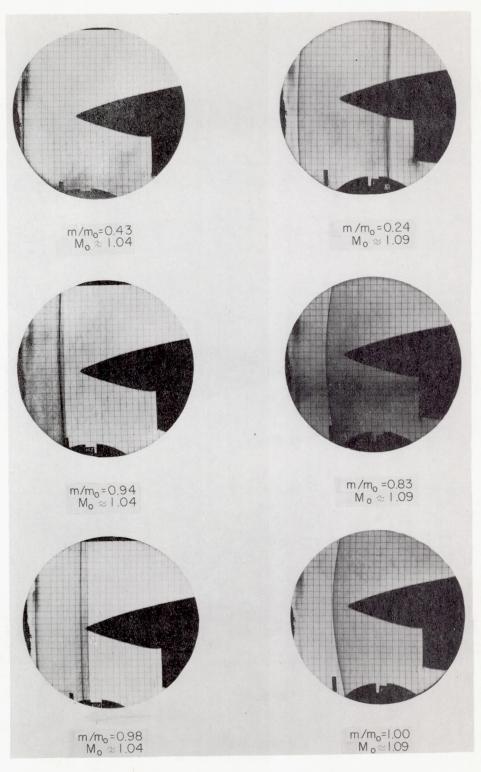
$M_0 = 1.09$

(a) Basic body, $\alpha = 0^O$.

L-77034
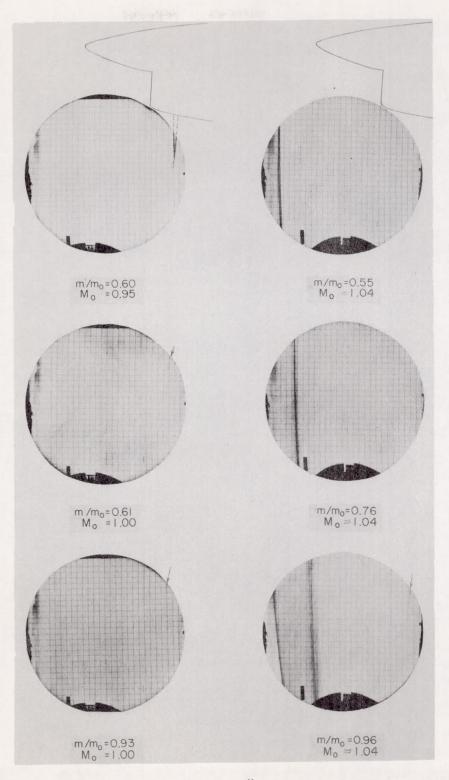
Figure 7.- Schlieren photographs of basic body and underslung scoop.

m/m$_0$=0.43
M$_0 \approx$ 1.04

m/m$_0$=0.24
M$_0 \approx$ 1.09

m/m$_0$=0.94
M$_0 \approx$ 1.04

m/m$_0$=0.83
M$_0 \approx$ 1.09

m/m$_0$=0.98
M$_0 \approx$ 1.04

m/m$_0$=1.00
M$_0 \approx$ 1.09

(b) Underslung scoop, $\alpha = 0^{\circ}$.

Figure 7.- Continued.

L-77035

m/m$_0$=0.60
M$_0$ =0.95

m/m$_0$=0.55
M$_0$ =1.04

m/m$_0$=0.61
M$_0$ =1.00

m/m$_0$=0.76
M$_0$ ≈1.04

m/m$_0$=0.93
M$_0$ =1.00

m/m$_0$=0.96
M$_0$ ≈1.04

(c) Underslung scoop, α ≈ 4°.

Figure 7.- Concluded.

L-77036

(a) $\alpha = 0^{\circ}$.
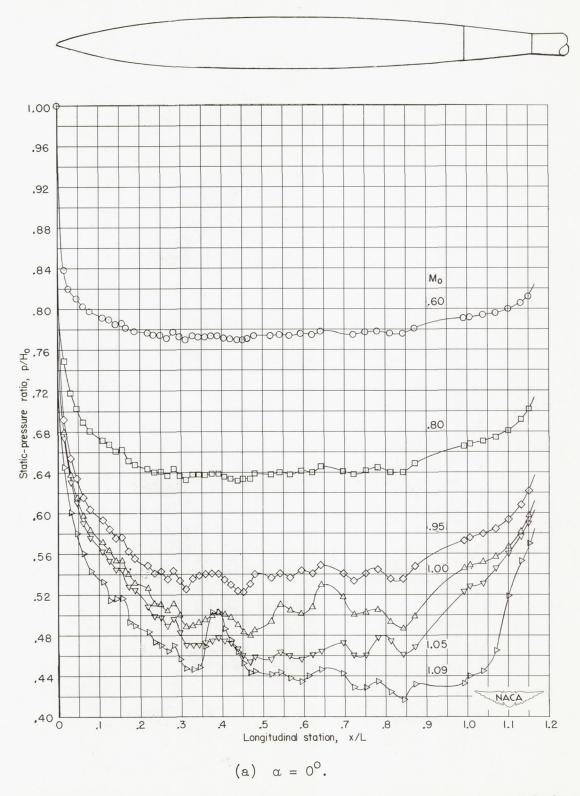
Figure 8.- Distributions of static pressure along top of basic model for
several stream Mach numbers.

(b) $\alpha \approx 10^{\circ}$.
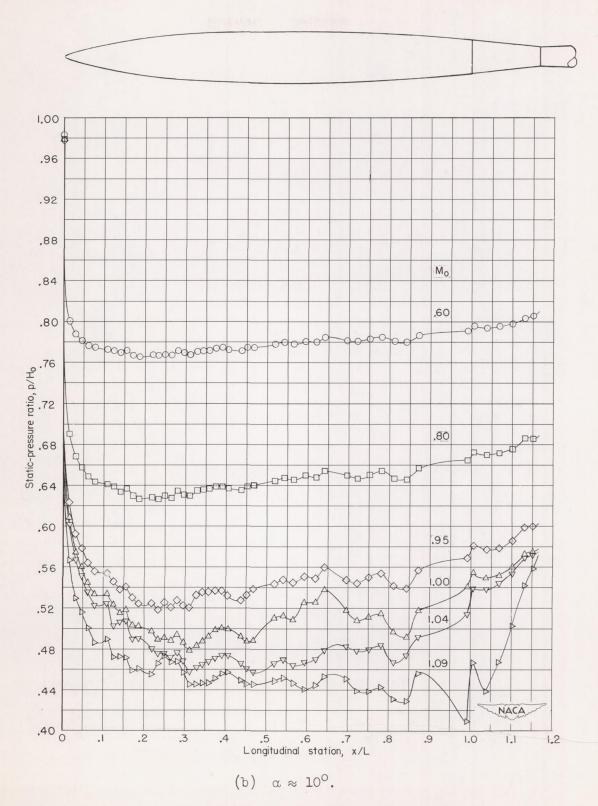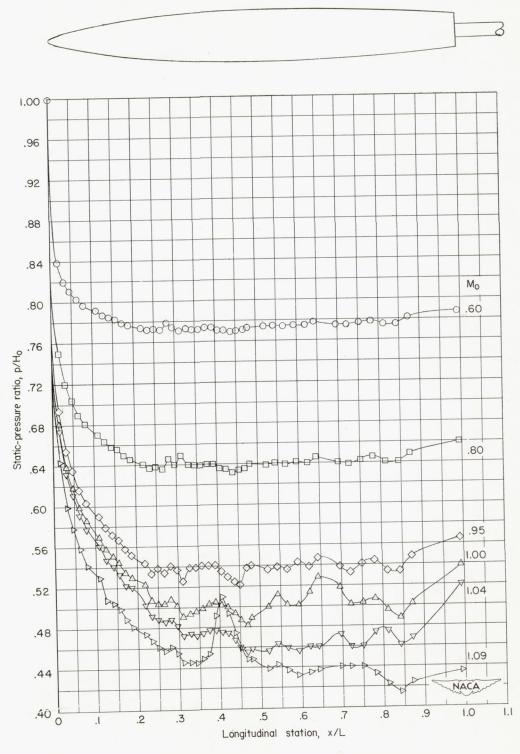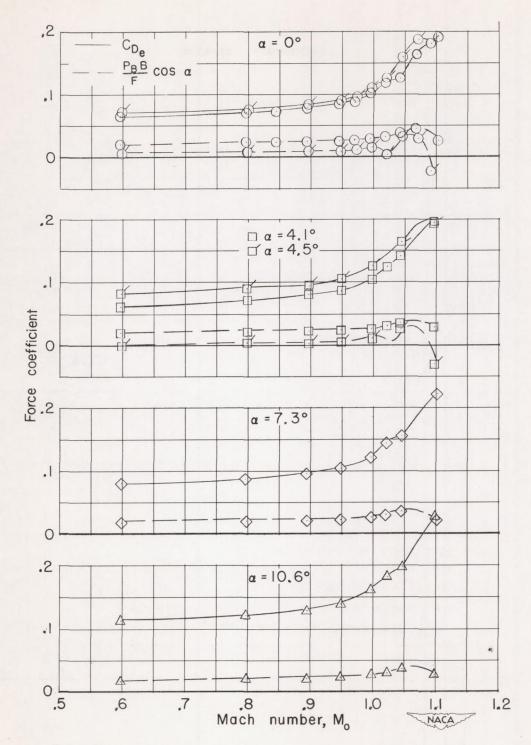
Figure 8.- Continued.
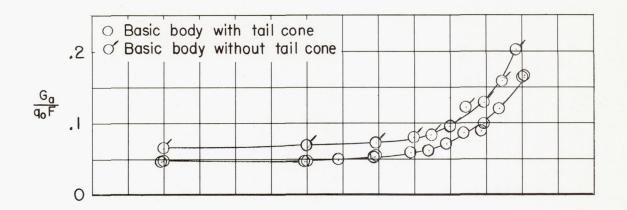
(c) Tail cone removed; $\alpha = 0°$.
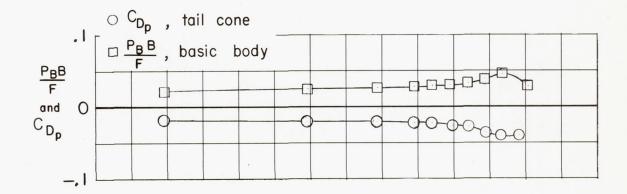
Figure 8.- Concluded.
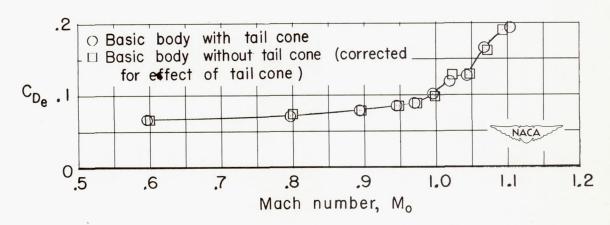
(a) Effect of angle of attack. Flagged symbols indicate
tail cone removed.

Figure 9.- Variation of external-force coefficient with stream Mach
number for basic body with and without tail cone.
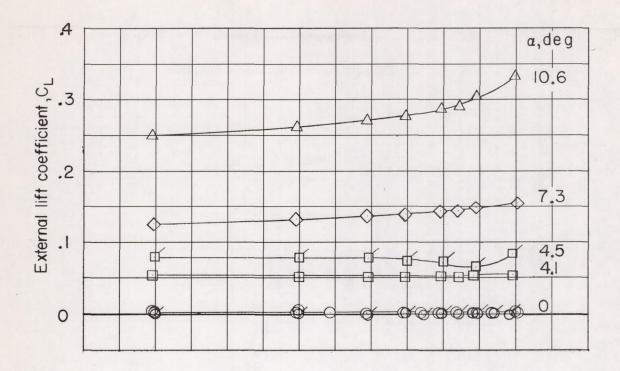
(b) Effect of tail cone; $\alpha = 0°$.

Figure 9.- Concluded.
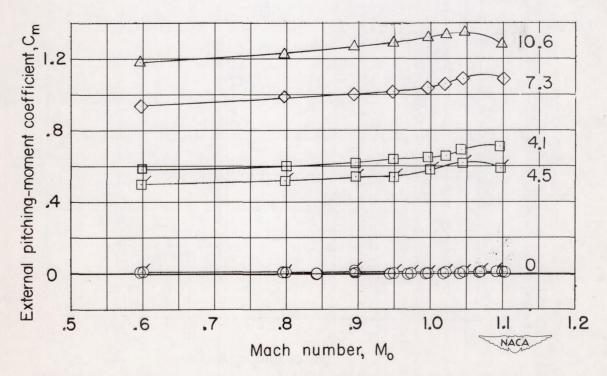
Figure 10.- Comparison of lift and pitching moment plotted against Mach
number for four angles of attack; basic body with and without tail
cone. Flagged symbols show tail cone removed.
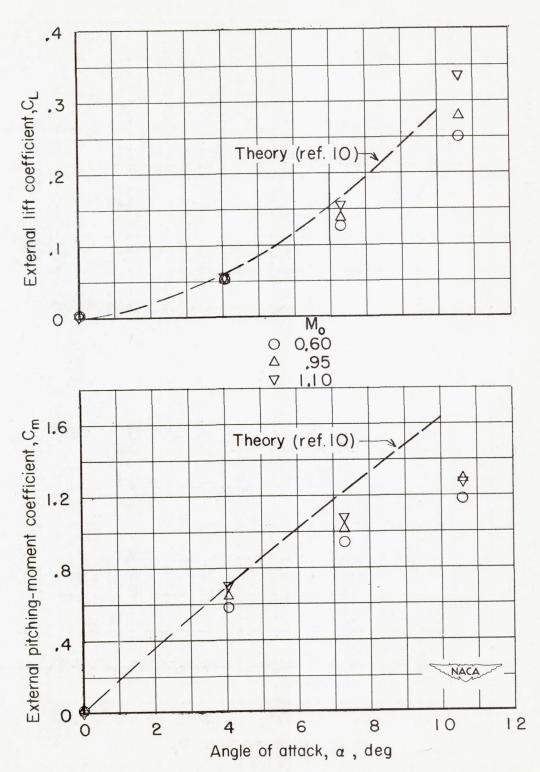
Figure 11.- Comparison of measured lift and pitching-moment coefficient plotted against angle of attack with theoretical values computed from reference 10.

(a) $M_O = 0.60$.
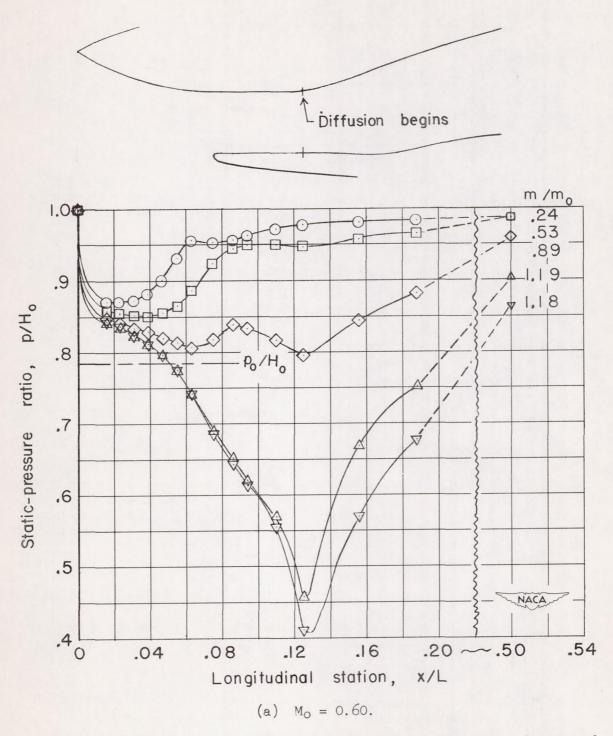
Figure 12.- Static-pressure distributions along center line of approach
   ramp and inner wall of diffuser for several Mach numbers and a range
   of mass-flow rates. $\alpha = 0^O$.

(b) $M_O = 0.80$.

Figure 12.- Continued.

Diffusion begins

(c) $M_0 = 0.95$.

Figure 12.- Continued.

(d) $M_O = 1.00.$
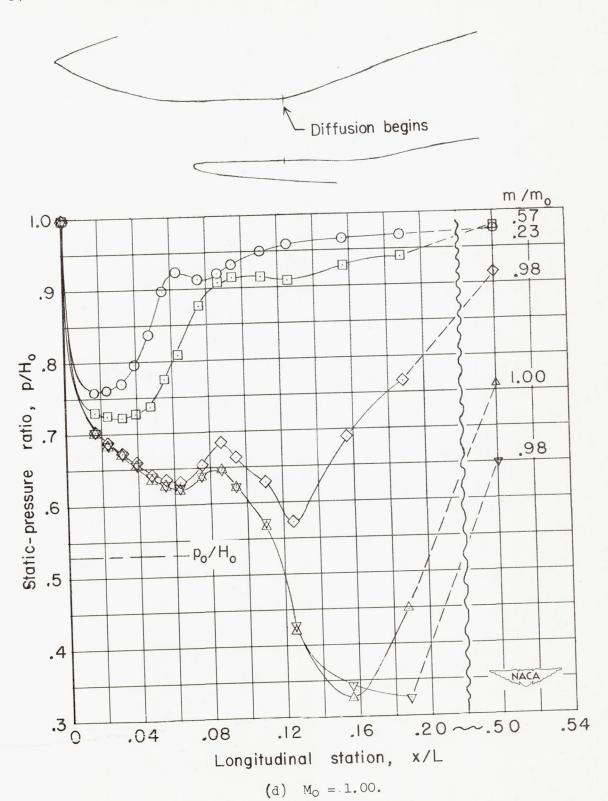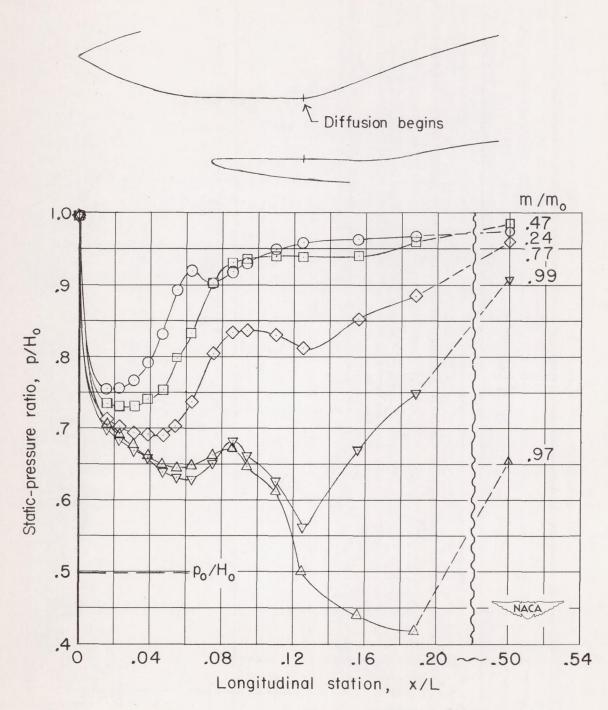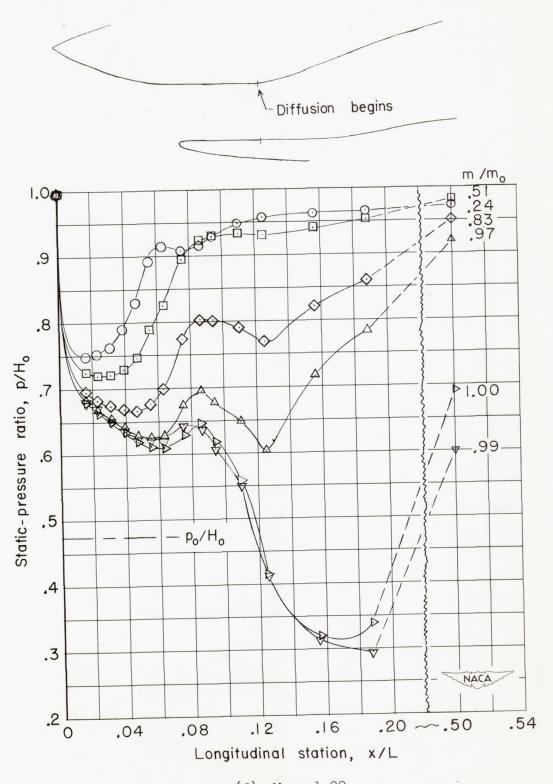
Figure 12.- Continued.

(e) $M_O \approx 1.04$.

Figure 12.- Continued.

(f) $M_0 \approx 1.09$.

Figure 12.- Concluded.

(a) $M_O = 0.60.$ (b) $M_O \approx 1.09.$
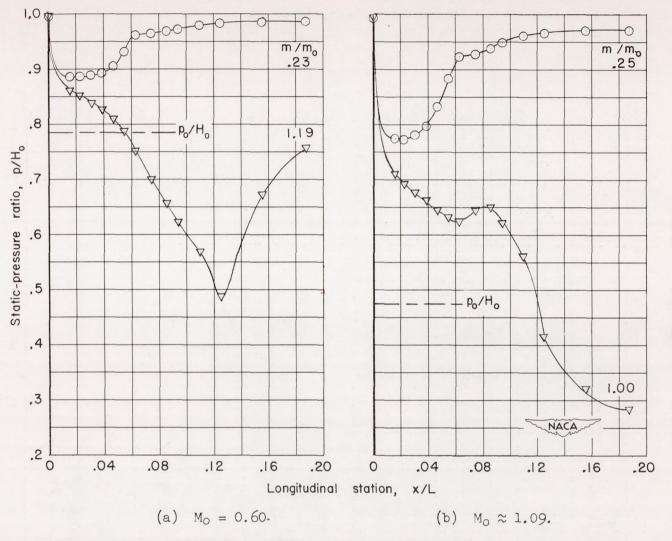
Figure 13.- Comparison of ramp-static-pressure distributions for the maximum and minimum test mass-flow rates. $\alpha \approx 4^o.$

(a) $M_O = 0.60$.

(b) $M_O \approx 1.09$.
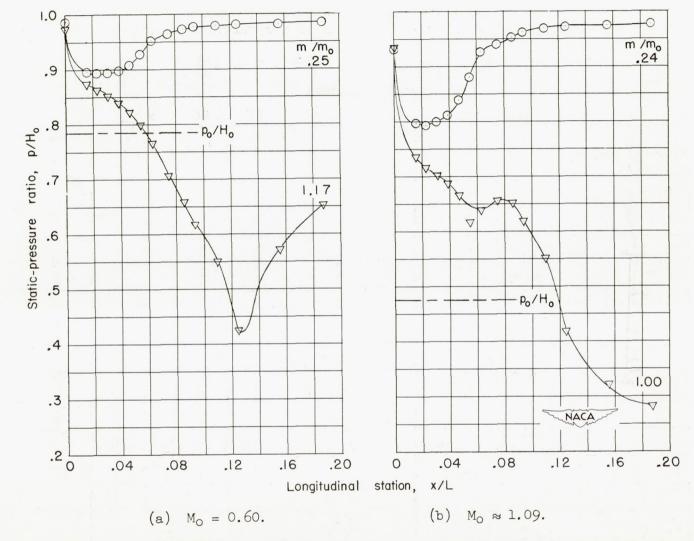
Figure 14.- Comparison of ramp-static-pressure distributions at the maximum
and minimum test mass-flow rates. $\alpha \approx 7°$.

(a) $M_O = 0.60$.

(b) $M_O = 0.80$.
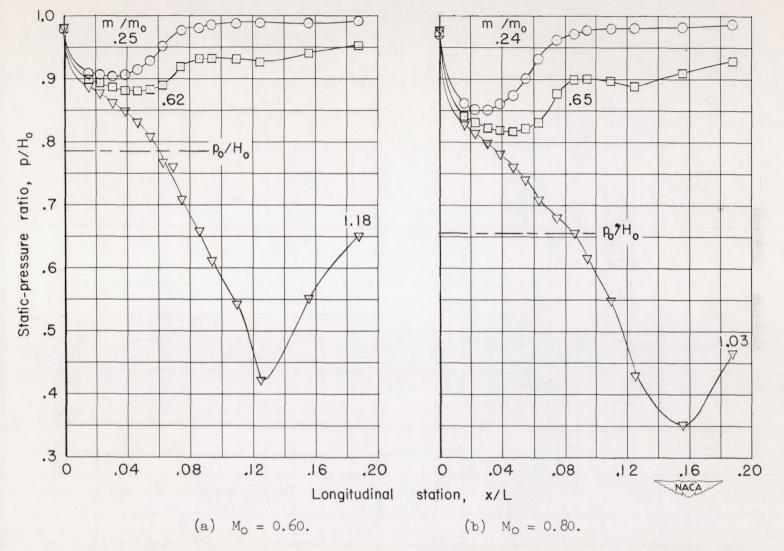
Figure 15.- Variation of static pressure along ramp at the model plane of symmetry for several mass-flow rates and Mach numbers. $\alpha \approx 10^o$.

Static-pressure ratio, p/H₀

1.0

m/m₀
.24

.9

.65

.8

.7

.6

p₀/H₀

.5

.4

1.00

.3

.2

0   .04   .08   .12   .16   .20

m/m₀
.24

.47

p₀/H₀

.99

NACA

0   .04   .08   .12   .16   .20

Longitudinal station, x/L

(c) M₀ = 0.95.

(d) M₀ = 1.00.
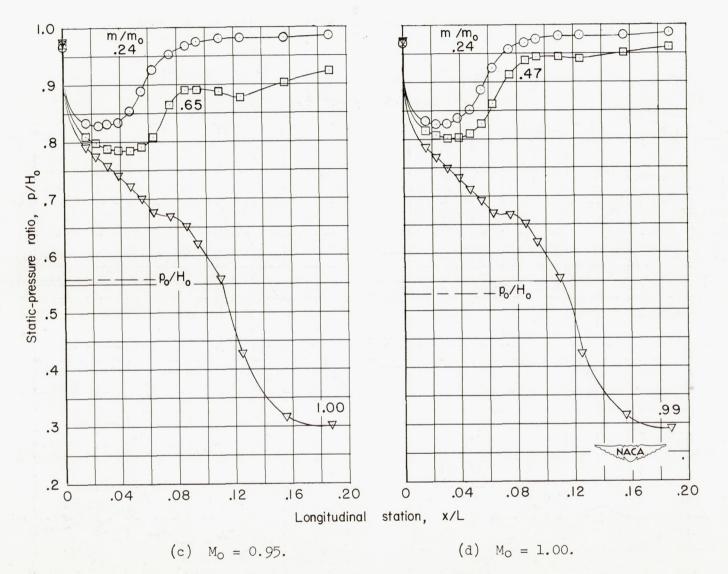
Figure 15.- Continued.

(e) $M_O \approx 1.05$.

(f) $M_O \approx 1.10$.
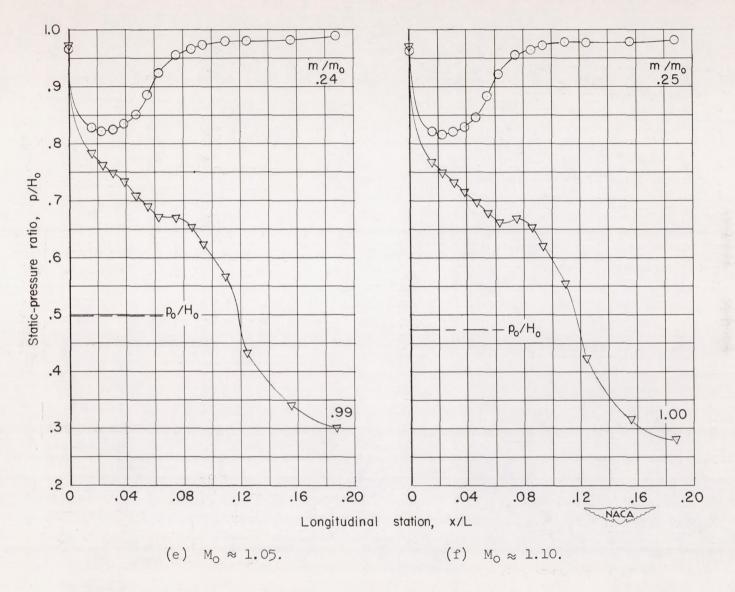
Figure 15.- Concluded.

(a) $\alpha = 0°$

(b) $\alpha \approx 10°$.
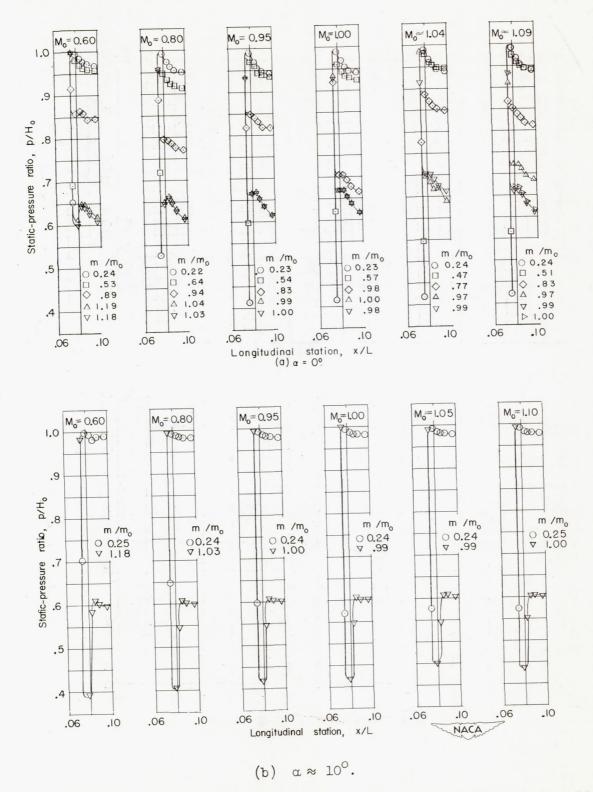
Figure 16.- Variations of static pressures on the inside of the inlet lip
at the center line.
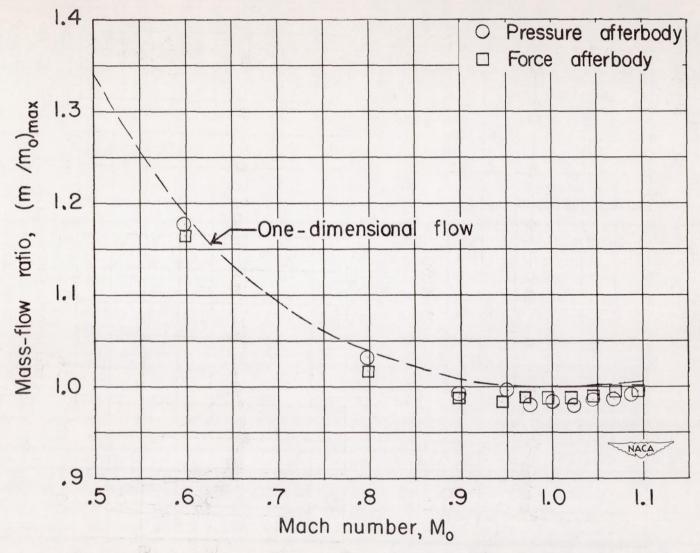
Figure 17.- Comparison of the maximum obtainable mass-flow from one-dimensional considerations with that obtained experimentally. $\alpha = 0°$.

Straight →

$M_0 = 0.60$

m/m_0
○ 0.24
□ .53
◇ .89
△ 1.19
▽ 1.18

$M_0 = 0.80$

m/m_0
○ 0.22
□ .64
◇ .94
△ 1.04
▽ 1.03

Static-pressure ratio, p/H_0

Longitudinal station, x/L

(a) $M_0 = 0.60$ and 0.80.
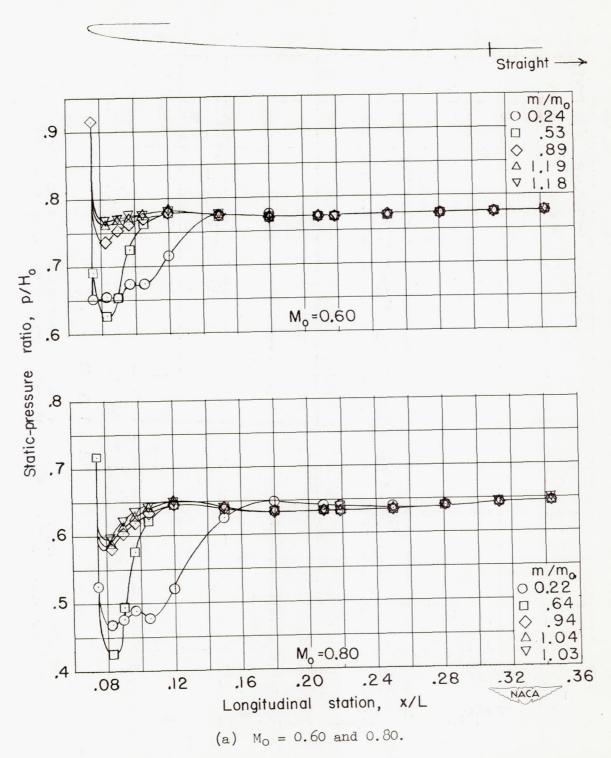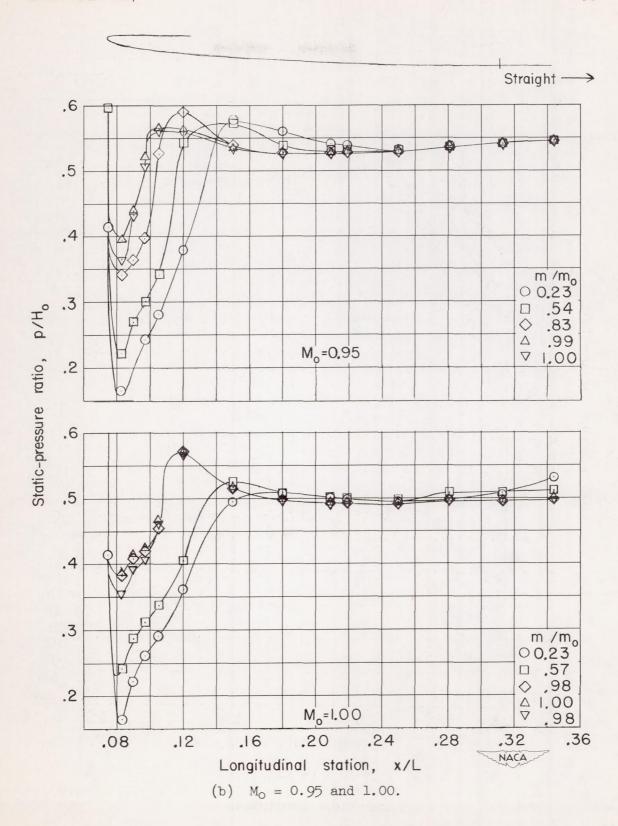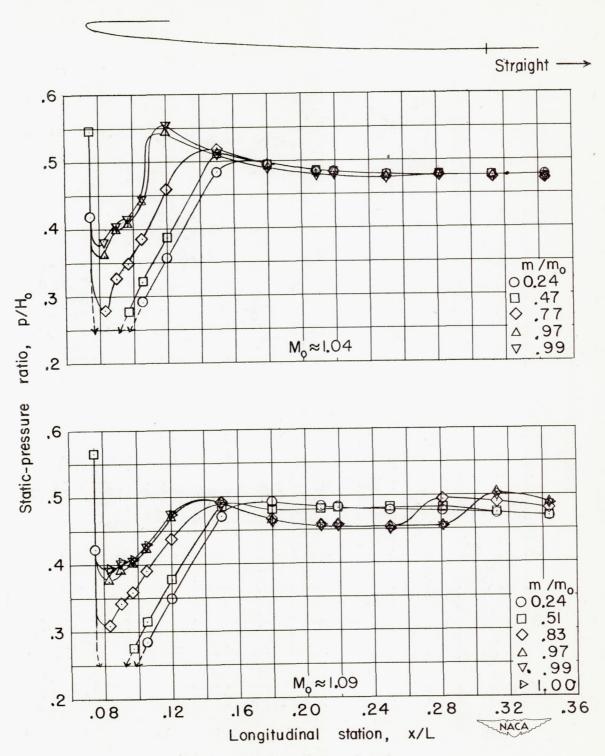
Figure 18.- Distribution of static pressures over outside of inlet lip at model plane of symmetry; $\alpha = 0^\circ$.

Straight ⟶

(b) M_O = 0.95 and 1.00.

(c) $M_0 \approx 1.04$ and 1.09.

Figure 18.- Concluded.
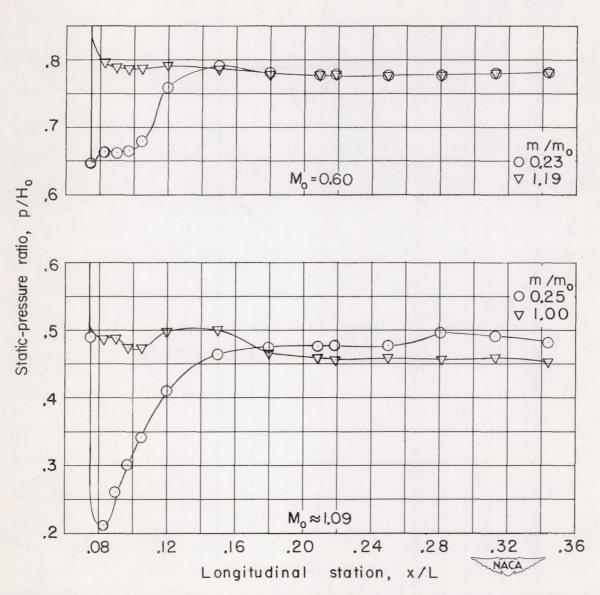
Figure 19.- Comparison of static-pressure distributions on the lip outside for the maximum and minimum test mass-flow rates. $\alpha \approx 4°$.
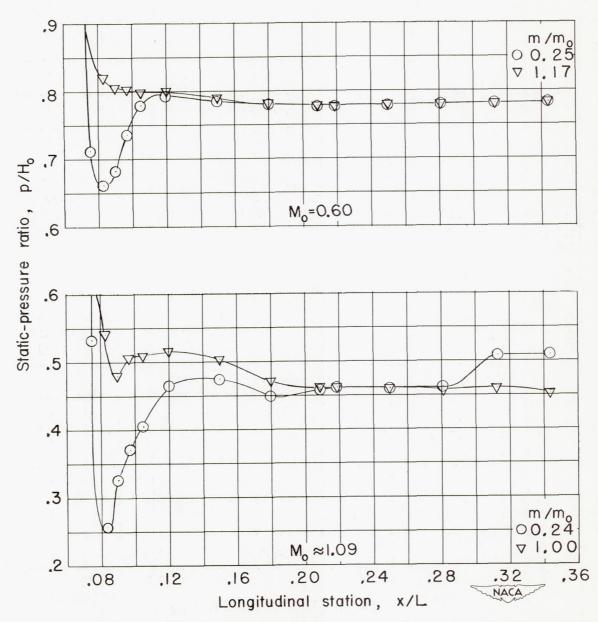
Figure 20.- Comparison of static pressure distributions on the lip outside
for the maximum and minimum test mass-flow rates. $\alpha \approx 7^\circ$.

(a) $M_O = 0.60$ and 0.80.
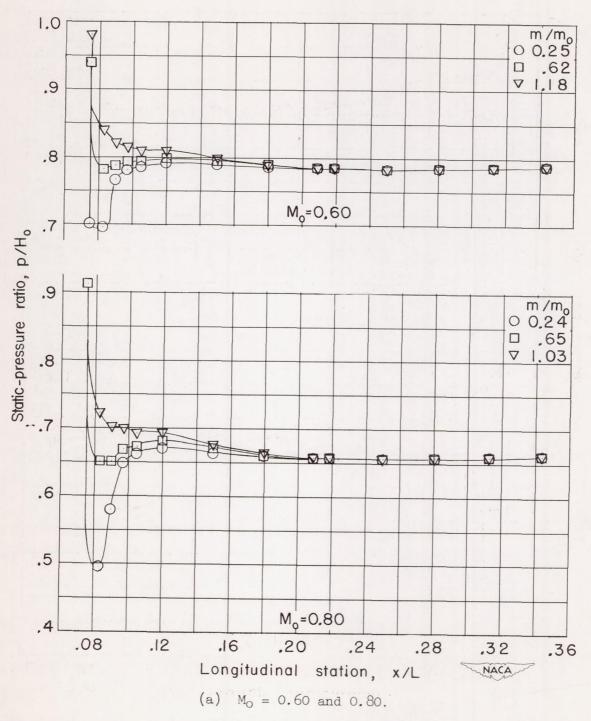
Figure 21.- Static pressure distributions over outside of inlet lip at
model plane of symmetry; $\alpha \approx 10^{\circ}$.

(b) $M_O = 0.95$ and 1.00.
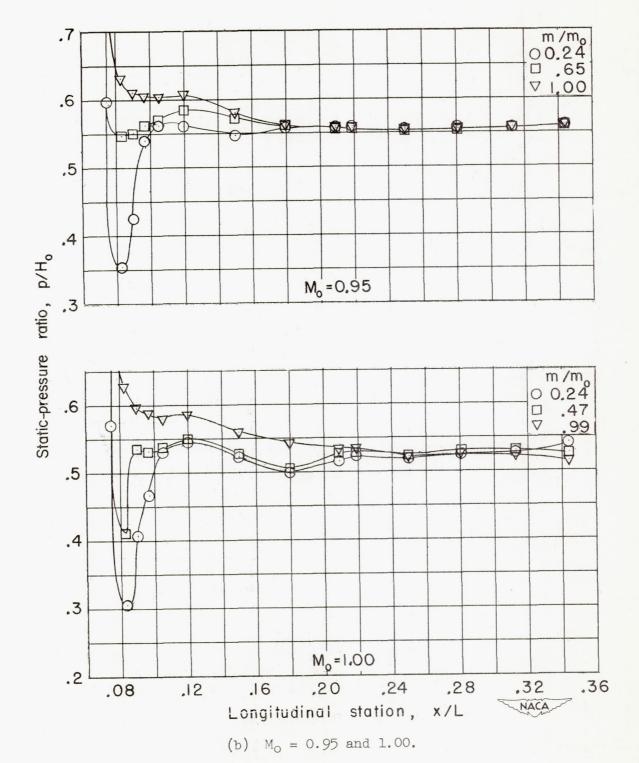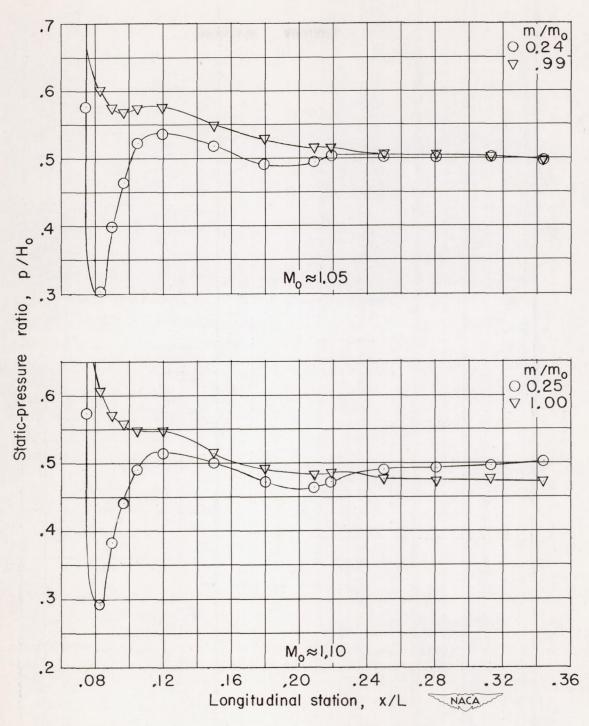
Figure 21.- Continued.

(c) $M_O \approx 1.05$ and 1.10.

Figure 21.- Concluded.

(a) $M_O = 0.60$.   (b) $M_O = 0.80$.
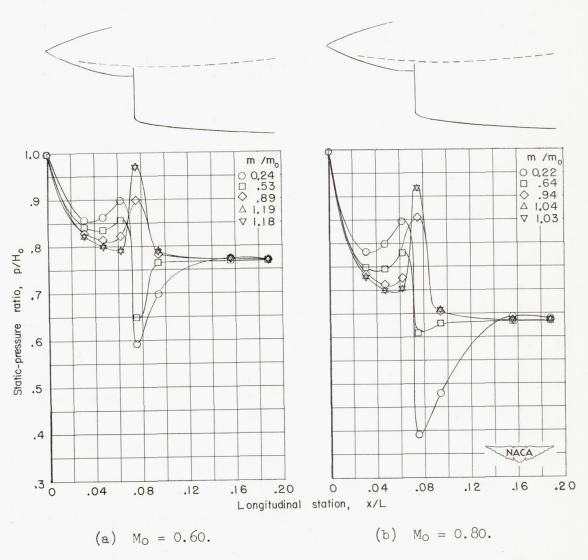
Figure 22.- Distribution of static pressure along gutter on right side
of model for several mass-flow rates. $\alpha = 0^O$.

(c) $M_O = 0.95.$ (d) $M_O = 1.00.$

Figure 22.- Continued.

(e) $M_O \approx 1.04.$ (f) $M_O \approx 1.09.$
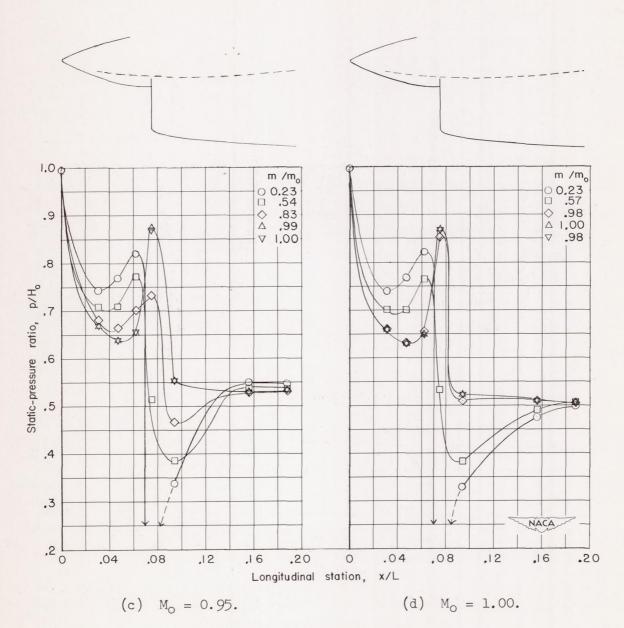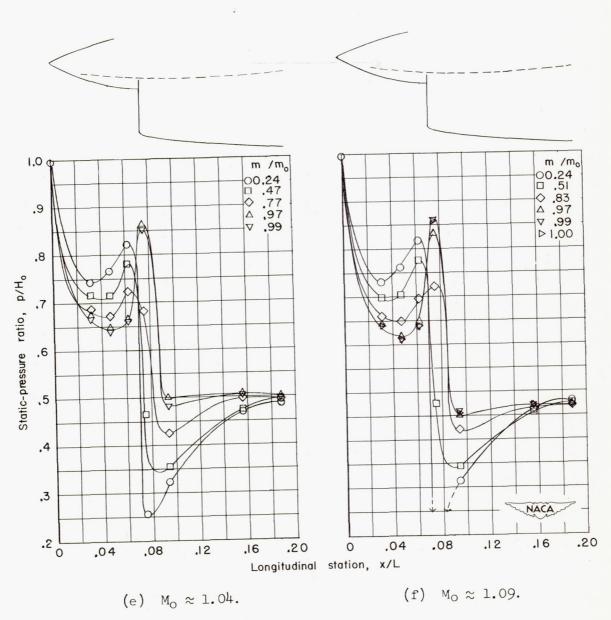
Figure 22.- Concluded.

(a) $M_O = 0.60$.

(b) $M_O \approx 1.09$.
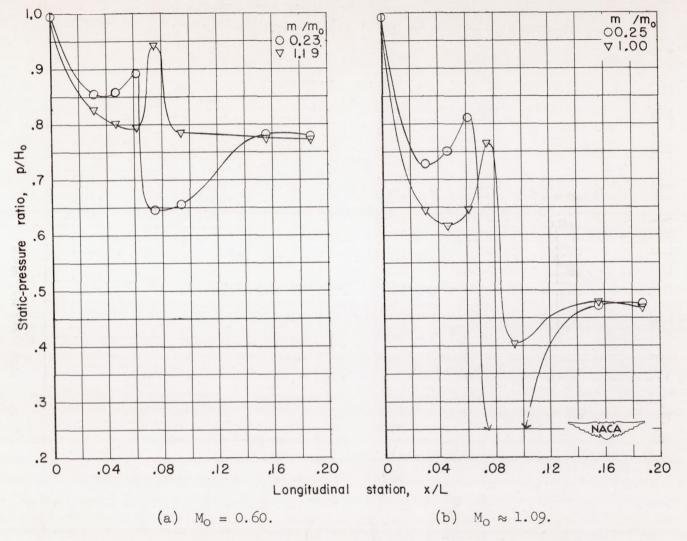
Figure 23.- Comparison of static pressures in gutter for maximum and minimum test mass-flow rates. $\alpha \approx 4^O$.

(a) $M_O = 0.60.$

(b) $M_O \approx 1.09.$
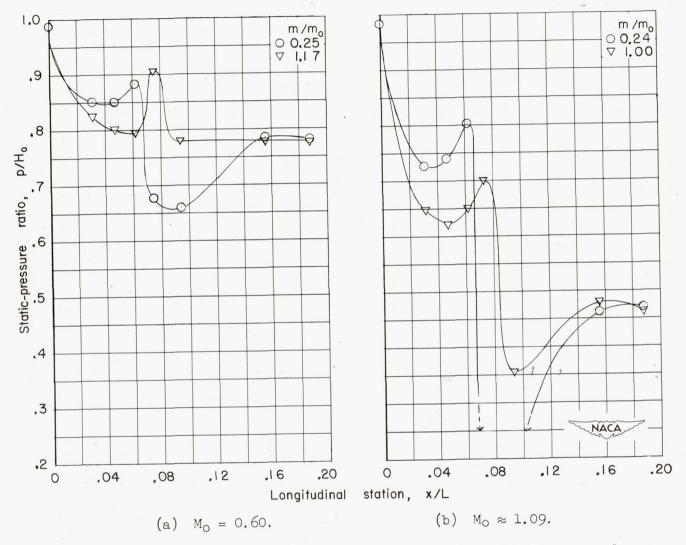
Figure 24.- Comparison of static pressures in gutter for maximum and
minimum test mass-flow rates. $\alpha = 7^O.$

(a) $M_O = 0.60$.   (b) $M_O = 0.80$.
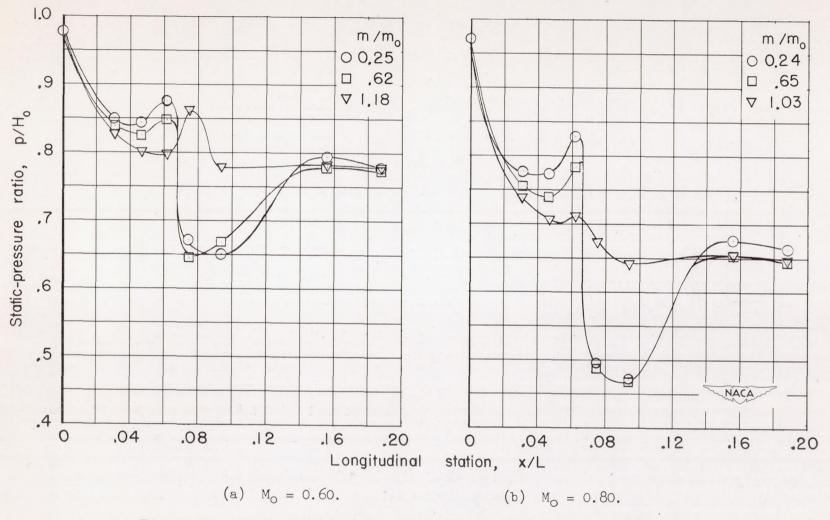
Figure 25.- Distribution of static pressure along gutter on right side of model for several mass-flow rates. $\alpha \approx 10^{\circ}$.

(c) $M_O = 0.95$.

(d) $M_O = 1.00$.
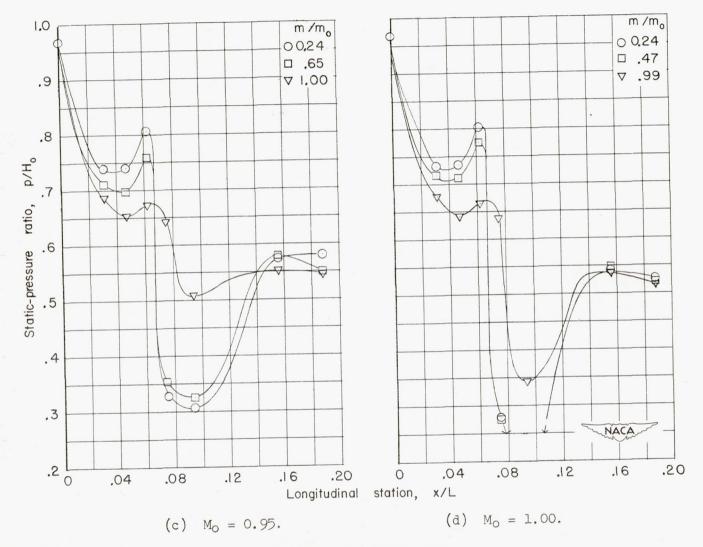
Figure 25.- Continued.

(e) $M_O \approx 1.05$.   (f) $M_O \approx 1.10$.
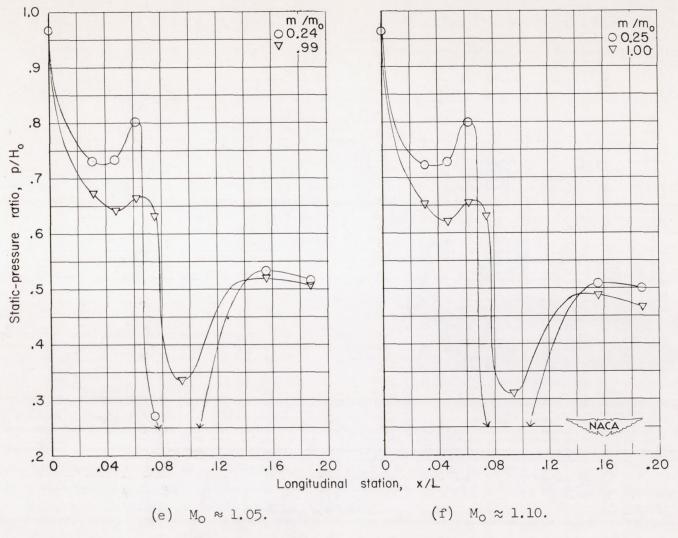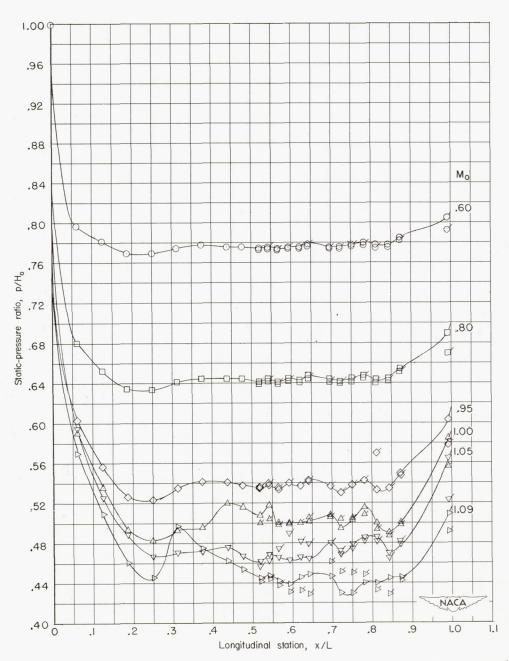
Figure 25.- Concluded.

(a) α = 0°. (Flagged symbols are for lowest mass-flow rate.)

Figure 26.- Comparison of static-pressure distributions along top of model;
maximum mass-flow rate.

(b) $\alpha \approx 4^{\circ}$.

Figure 26.- Continued.

(c) $\alpha \approx 7°$.

Figure 26.- Continued.

(d) $\alpha \approx 10^{\circ}$.
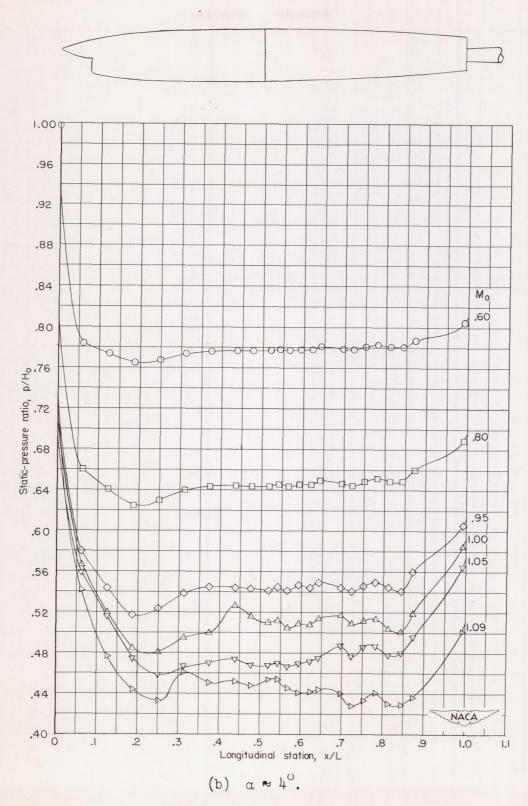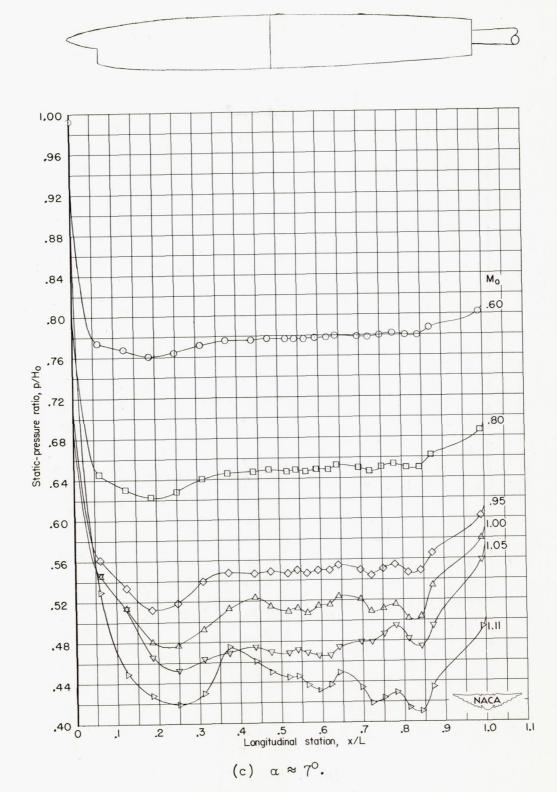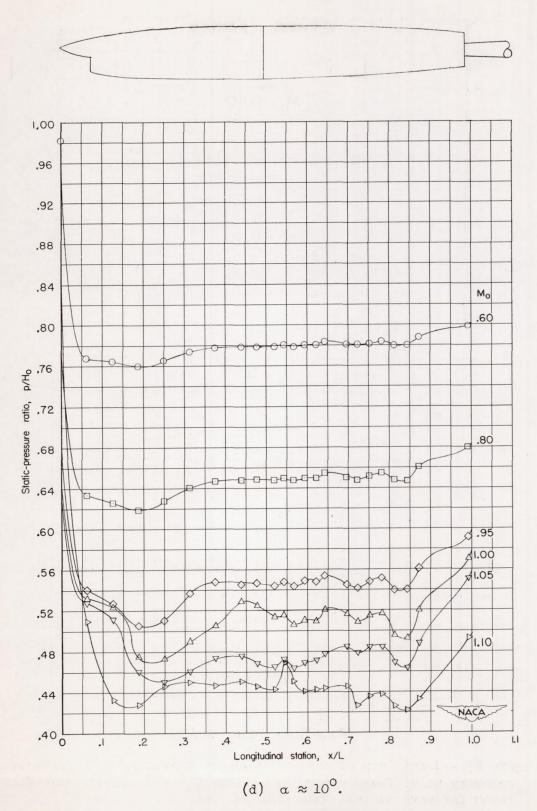
Figure 26.- Concluded.
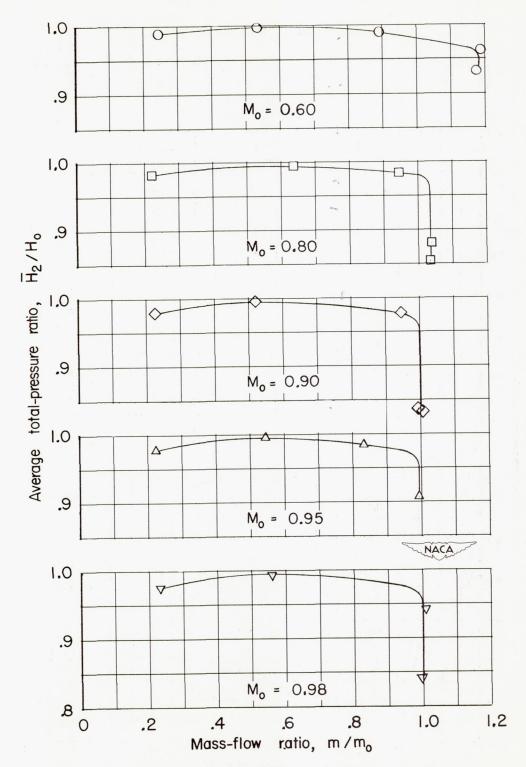
Figure 27.- Comparison of mass-flow-weighted average total pressure
recovery at diffuser measuring station plotted against mass-flow
ratio for several test Mach numbers. $\alpha = 0^o$.
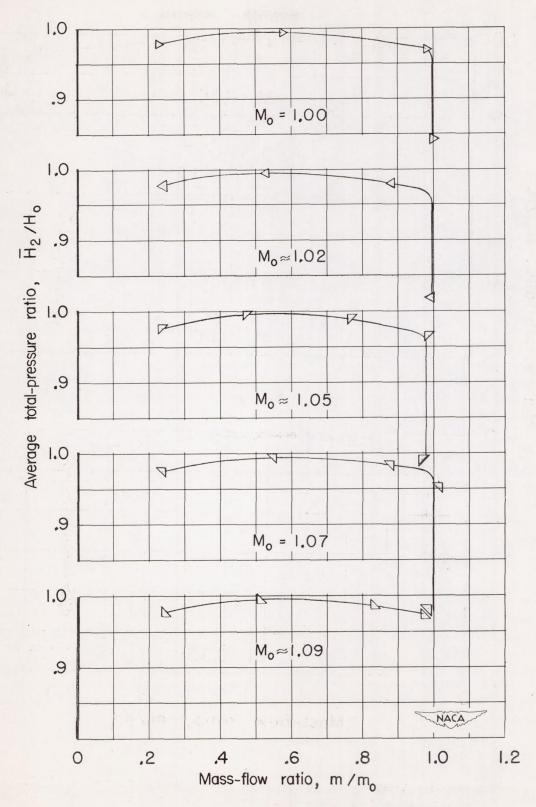
Figure 27.- Concluded.

(a) $M_0 = 0.60$, 0.80, and 0.95.
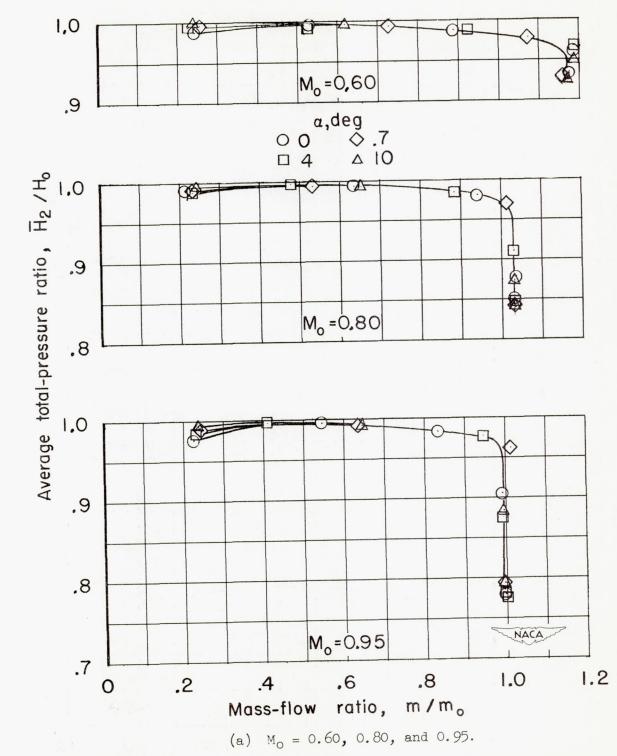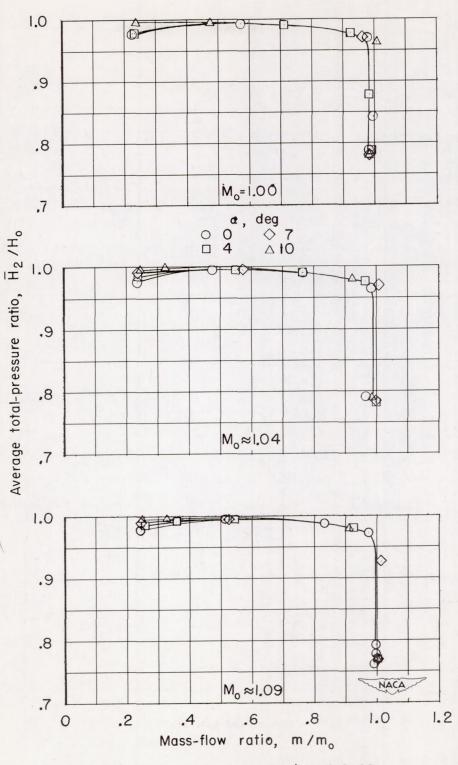
Figure 28.- Comparison of average total pressure ratio at diffuser measuring station mass-flow ratio for four test angles of attack.

(b) $M_O = 1.00$; $M_O \approx 1.04$ and 1.09.

Figure 28.- Concluded.
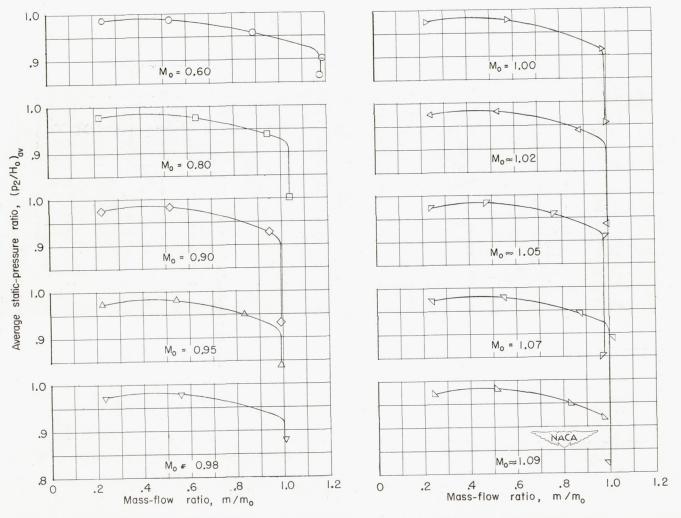
Figure 29.- Variation of average static-pressure recovery ratio at diffuser measurement station with mass-flow ratio for several Mach numbers. $\alpha = 0^{\circ}$.

(a) $M_O = 0.60$, 0.80, and 0.95.
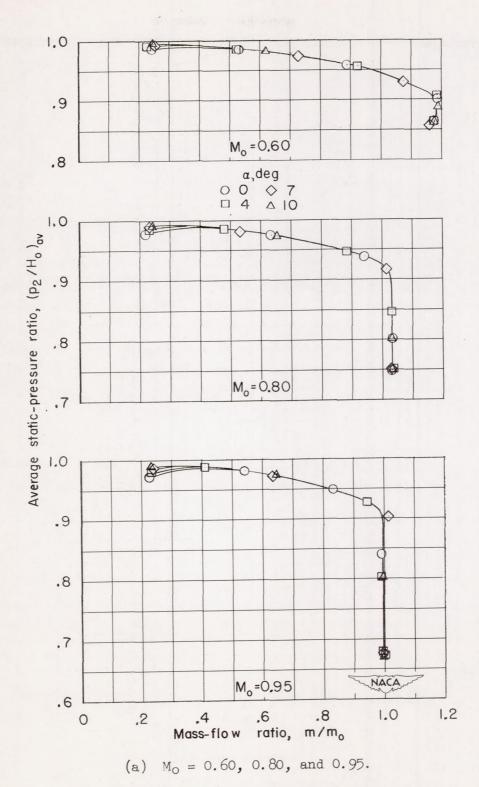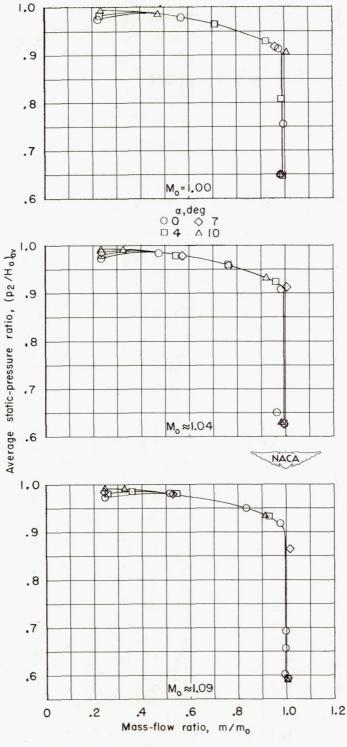
Figure 30.- Comparison of average static-pressure ratios at end of diffuser for four test angles of attack.

(b) $M_O = 1.00$; $M_O \approx 1.04$ and 1.09.

Figure 30.- Concluded.
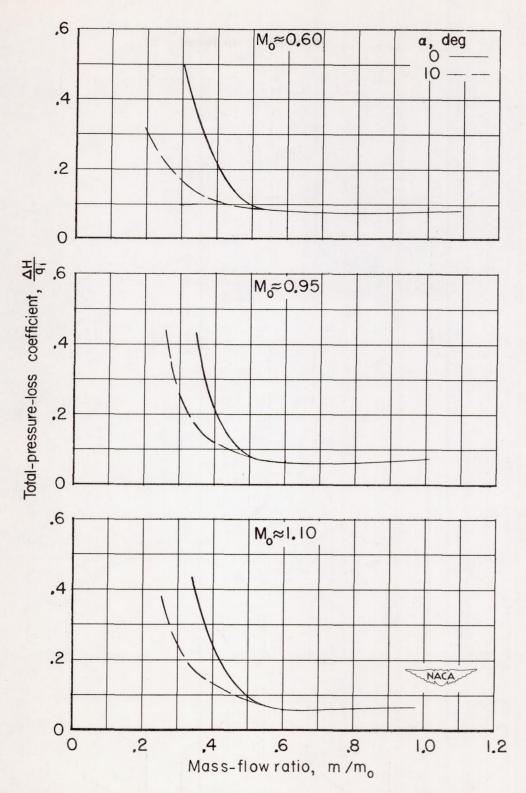
Figure 31.- Effect of mass flow and angle of attack on internal duct losses.
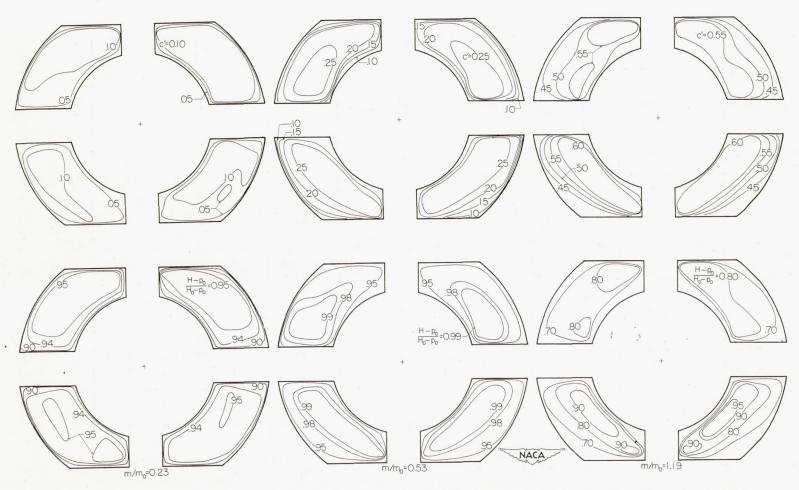
Figure 32.- Distributions of mass flow and impact-pressure ratio at end of diffuser. $M_O = 0.60$; $\alpha = 0°$.
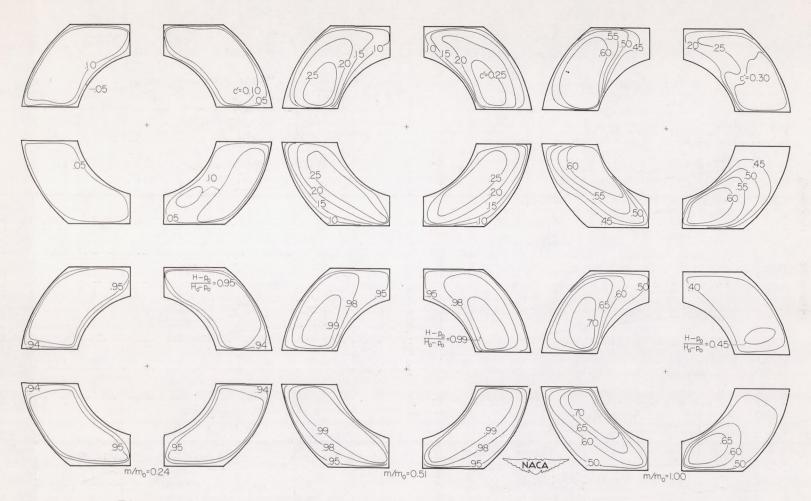
Figure 33.- Distributions of mass flow and impact-pressure ratio at end of diffuser. $M_O \approx 1.09$; $\alpha = 0^O$.
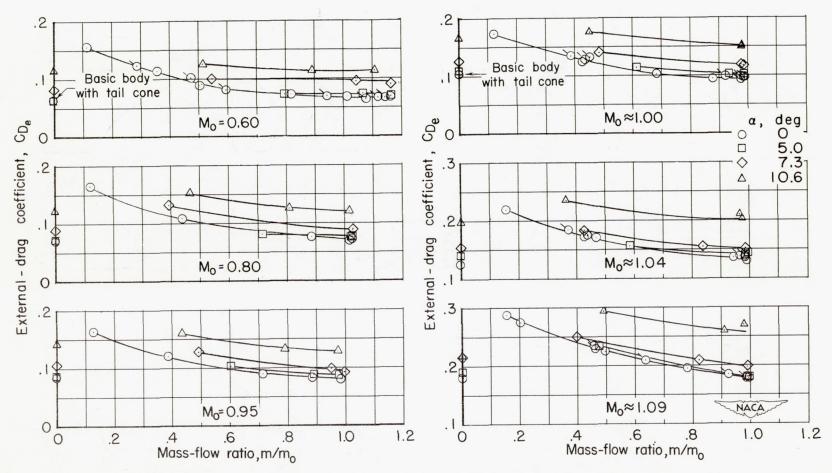
Figure 34.- Variation of external drag with mass-flow ratio at four test angles of attack. Flagged symbols indicate repeat points.
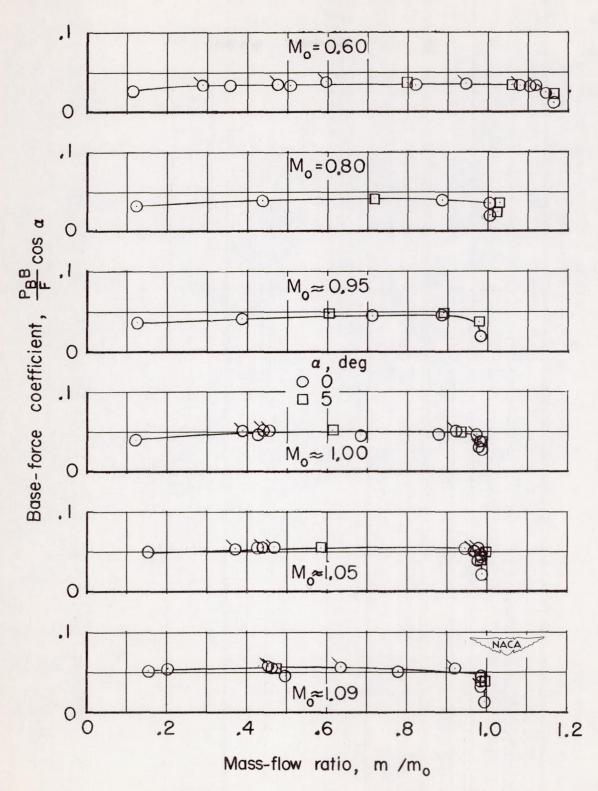
Figure 35.- Comparison of base force coefficients for $\alpha = 0^\circ$ and $\alpha = 5^\circ$ for several stream Mach numbers. Flagged symbols indicate repeat points.

(a) $M_O = 0.60$.   (b) $M_O = 0.80$.   (c) $M_O \approx 0.95$.
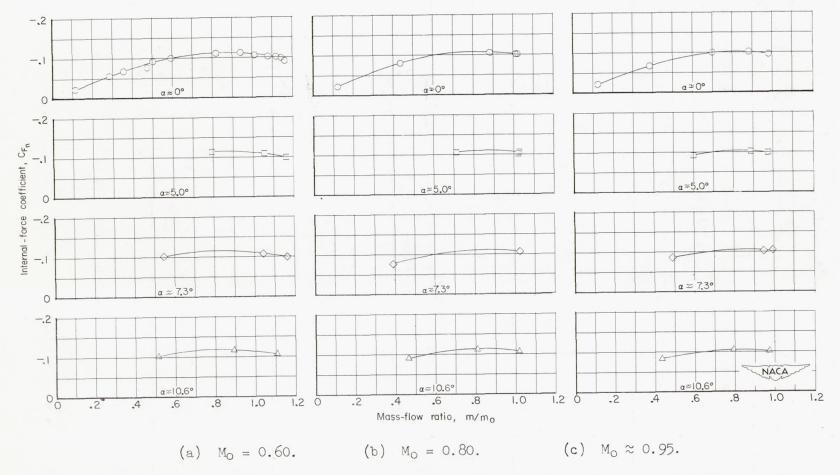
Figure 36.- Comparison of internal-force coefficient with mass-flow ratio
for four test angles of attack.

(d) $M_O \approx 1.00.$ (e) $M_O \approx 1.04.$ (f) $M_O \approx 1.09.$
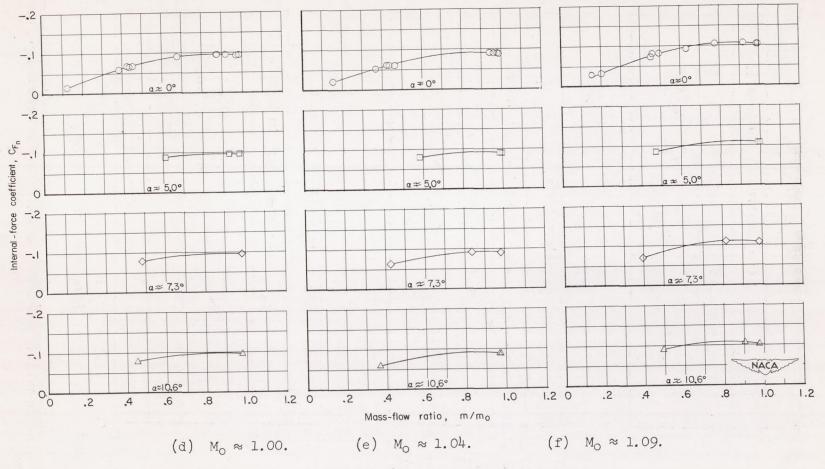
Figure 36.- Concluded.
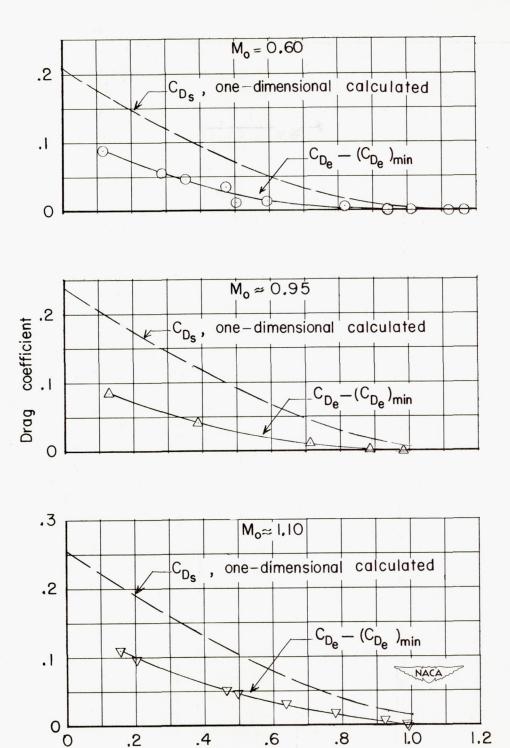
Figure 37.- Comparison of variation of external-drag increment calculated from one-dimensional considerations and that obtained experimentally. $\alpha = 0°$.
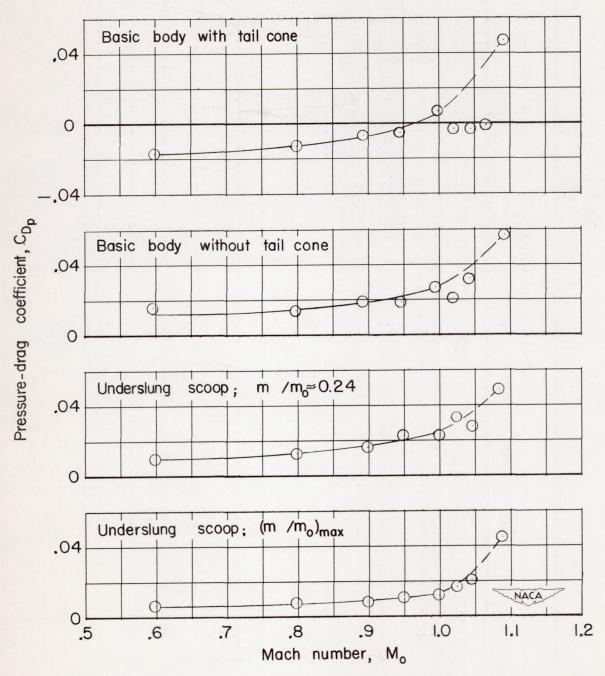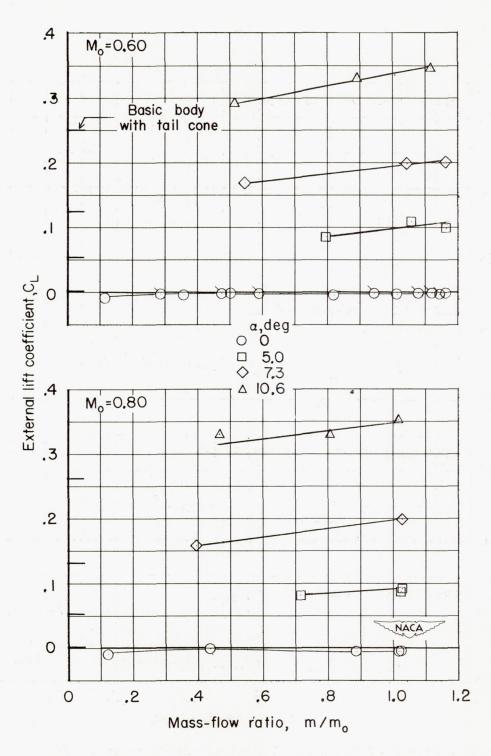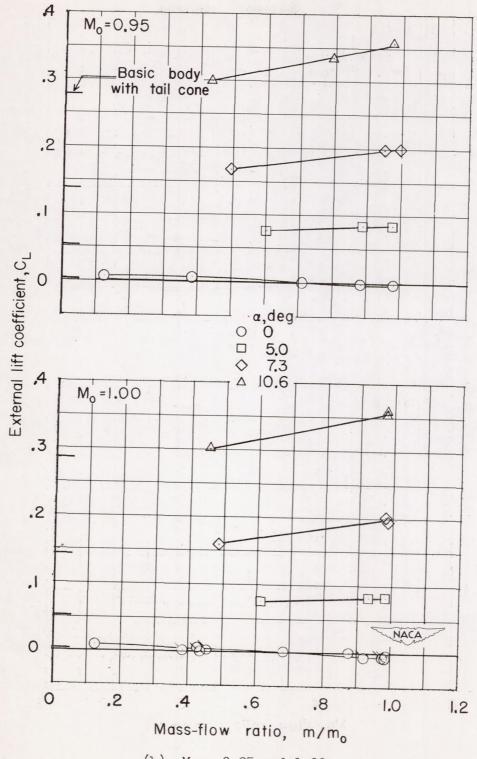
Figure 38.- Effect of internal flow on afterbody pressure drag. $\alpha = 0^{\circ}$.
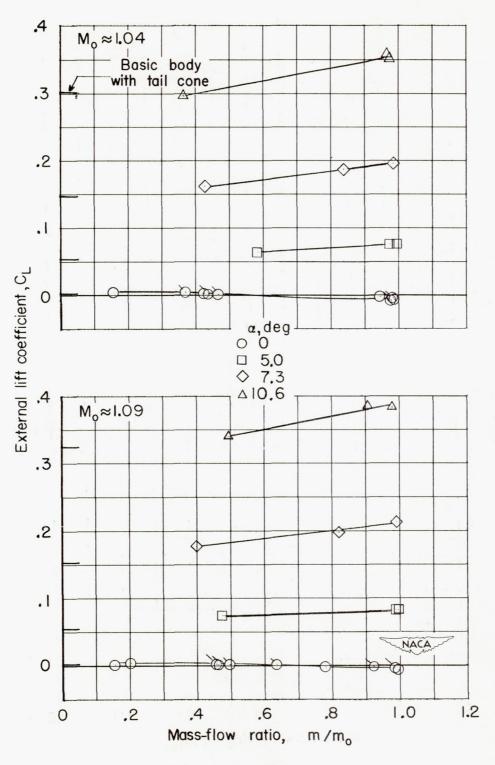
(a) M_O = 0.60 and 0.80.

Figure 39.- Variation of external lift coefficient with mass-flow ratio
     for four test angles of attack. Flagged symbols indicate repeat points.
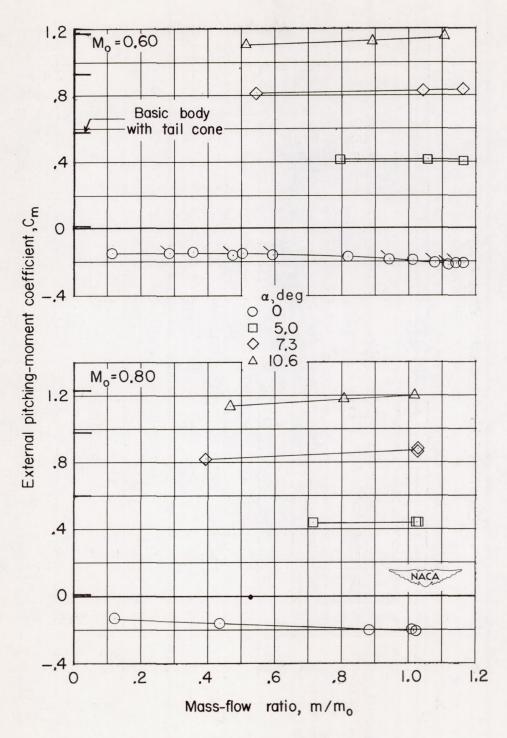
(b) $M_0 = 0.95$ and 1.00.

Figure 39.- Continued.
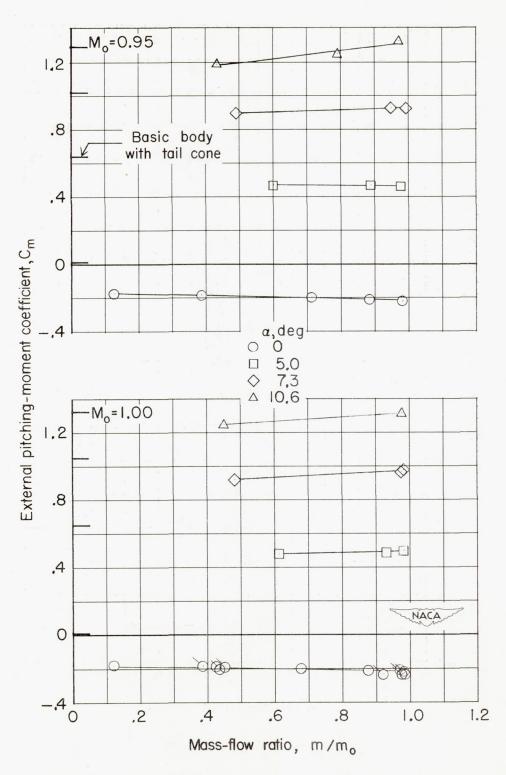
(c) $M_O \approx 1.04$ and 1.09.
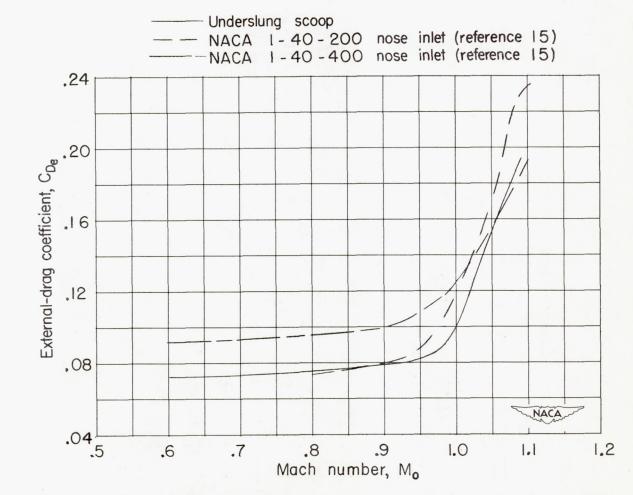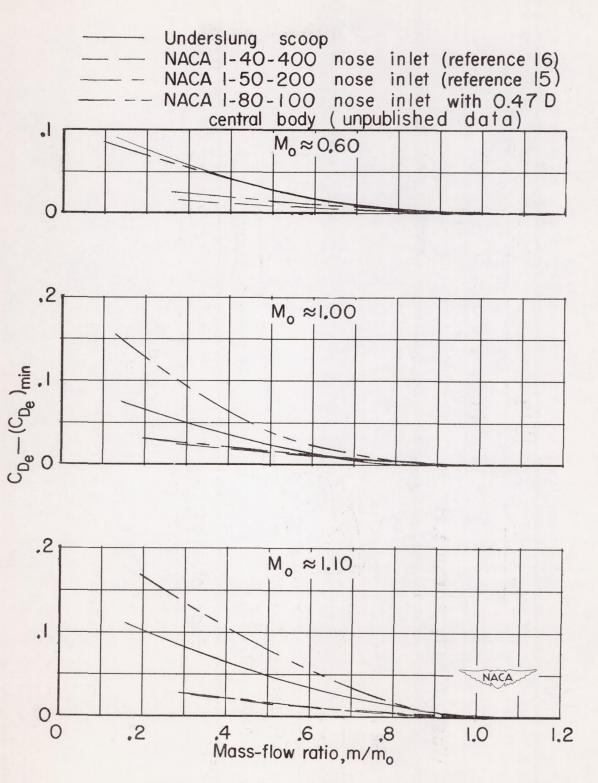
Figure 39.- Concluded.
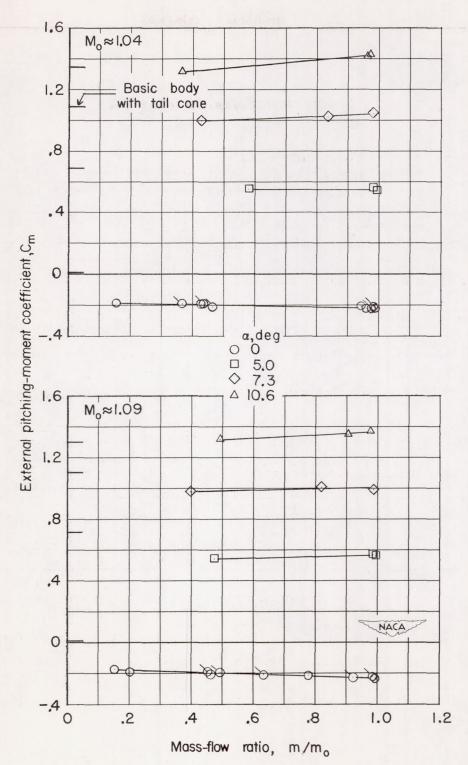
(a) M_O = 0.60 and 0.80.

Figure 40.- Variation of external pitching-moment coefficient versus mass-flow ratio for four test angles of attack. Flagged symbols indicate repeat points.

(b) $M_O = 0.95$ and 1.00.

Figure 40.- Continued.
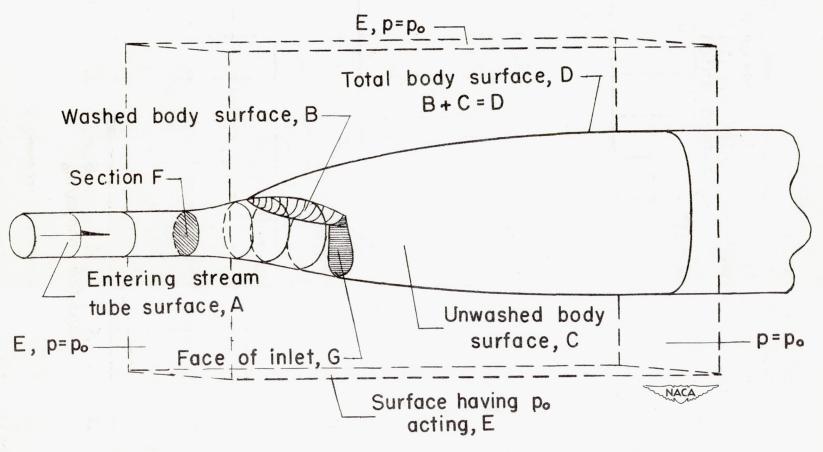
(c) $M_O \approx 1.04$ and 1.09.

Figure 40.- Concluded.

Figure 41.- Comparison of external drag against Mach number for the underslung scoop. $\alpha = 0^\circ$; $\frac{m}{m_0} = 0.8$.

(a) Measured external-drag increments.

Figure 42.- Effects of mass-flow ratio on external drag.

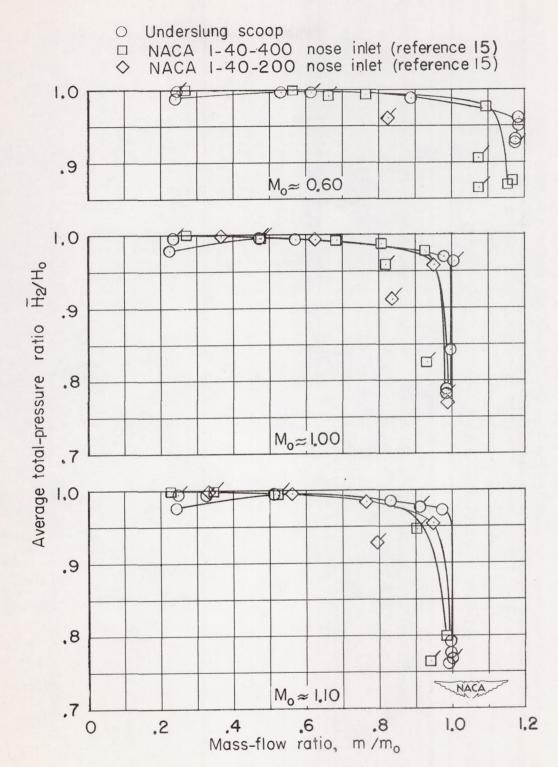(b) Momentum-theorem control surfaces for qualitative drag evaluation.

Figure 42.- Concluded.

Figure 43.- Comparison of total pressure recovery with several series 1 open-nose inlets tested on similar afterbodies. $\alpha = 0^O$; $\alpha \approx 10^O$. (Flagged symbols indicate $\alpha \approx 10^O$.)